3-1-2018

Space-based Maneuver Detection and Characterization using Multiple Model Adaptive Estimation

Justin D. Katzovitz

Follow this and additional works at: https://scholar.afit.edu/etd

Part of the Astrodynamics Commons, and the Space Vehicles Commons

SPACE-BASED MANEUVER DETECTION AND CHARACTERIZATION USING MULTIPLE MODEL ADAPTIVE ESTIMATION

THESIS

Justin D. Katzovitz, 2d Lt, USAF

AFIT-ENY-MS-18-M-268

DEPARTMENT OF THE AIR FORCE
AIR UNIVERSITY

AIR FORCE INSTITUTE OF TECHNOLOGY

Wright-Patterson Air Force Base, Ohio

DISTRIBUTION STATEMENT A. APPROVED FOR PUBLIC RELEASE;

DISTRIBUTION IS UNLIMITED

AFIT-ENY-MS-18-M-268

SPACE-BASED MANEUVER DETECTION AND CHARACTERIZATION

USING MULTIPLE MODEL ADAPTIVE ESTIMATION

THESIS

Presented to the Faculty

Department of Aeronautics and Astronautics

Graduate School of Engineering and Management

Air Force Institute of Technology

Air University

Air Education and Training Command

in Partial Fulfillment of the Requirements for the

Degree of Master of Science in Astronautical Engineering

Justin D. Katzovitz, BS

2d Lt, USAF

March 2018

AFIT-ENY-MS-18-M-268

SPACE-BASED MANEUVER DETECTION AND CHARACTERIZATION

USING MULTIPLE MODEL ADAPTIVE ESTIMATION

Justin D. Katzovitz, BS
2d Lt, USAF

Approved:

Joshuah A. Hess, PhD (Chairman)	Date
Richard G. Cobb, PhD (Member)	Date
Kirk W. Johnson, PhD (Member)	Date

AFIT-ENY-MS-18-M-268

Abstract

An increasingly congested space environment requires real-time and dynamic space situational awareness (SSA) on both domestic and foreign space objects in Earth orbits. Current statistical orbit determination (SOD) techniques are able to estimate and track trajectories for cooperative spacecraft. However, a non-cooperative spacecraft performing unknown maneuvers at unknown times can lead to unexpected changes in the underlying dynamics of classical filtering techniques. Adaptive estimation techniques can be utilized to build a bank of recursive estimators with different hypotheses on a system's dynamics. The current study assesses the use of a multiple model adaptive estimation (MMAE) technique for detecting and characterizing non-cooperative spacecraft maneuvers using space-based sensors for spacecraft in close proximity. A series of classical and variable state multiple model frameworks are implemented, tested, and analyzed through maneuver detection scenarios using relative spacecraft orbit dynamics. Variable levels of noise, data availability, and target thrust profiles are used to demonstrate and quantify the performance of the MMAE algorithm using Monte Carlo methods. The current research demonstrates that adaptive estimation techniques are able to handle unknown changes in the dynamics while keeping comparable errors with respect to other classical estimation methods.

To those who made the ultimate sacrifice so others could reach for the stars

Ad Astra Per Aspera

Acknowledgements

There are many people that I must recognize without whom I believe this journey through AFIT and beyond would not be possible.

To my research advisor, Joshuah Hess, who has kept me on track and guided me through my thesis project every step of the way.

To my instructors and advisors at AFIT and USAFA, who inspire me to continue learning not just throughout my career but throughout my life.

To my parents, Larry and Kristina, who have provided me with every opportunity to aspire to greatness and a moral foundation to use that greatness for good.

To my sister, Louise, who excites my inner passion for engineering and constantly reminds me that I could be making more money in the private sector.

To my lovely wife, Felicia, who not only supports me through the toughest times but is there to pick me up and celebrate the happiest times.

<div align="right">Justin D. Katzovitz</div>

Table of Contents

List of Figures

List of Tables

List of Acronyms

U.S.   United States

UN   United Nations

USAF   U.S. Air Force

DoD   U.S. Department of Defense

SSA   space situational awareness

JSpOC   Joint Space Operations Center

SSN   Space Surveillance Network

AFSPC   Air Force Space Command

NRC   National Research Council

UCT   uncorrelated target

RPO   rendezvous and proximity operations

GEO   geosynchronous orbit

SOD   statistical orbit determination

MMSE   minimum mean square error

LEO   low Earth orbit

BLS   batch least squares

KF   Kalman filter

EKF   extended Kalman filter

MMAE   multiple model adaptive estimation

IMM   interacting multiple models

UKF   unscented Kalman filter

UT   unscented transformation

FES   fixed epoch smoothers

IMM   interacting multiple models

PDF   probability density function

VSD   variable state dimension

MD   Mahalanobis distance

ED   Euclidean distance

NMC   natural motion circumnavigation

ROEs   relative orbital elements

EO   electro-optical

LIDAR   light detection and ranging

IOD   initial orbit determination

1G   first generation

2G   second generation

SPACE-BASED MANEUVER DETECTION AND CHARACTERIZATION

USING MULTIPLE MODEL ADAPTIVE ESTIMATION

I. Introduction

1.1 Motivation

Since launching the first satellites into Earth orbit, the United States (U.S.) and its military have treated the space domain as the ultimate high ground [1]. The space-based technology requirements of today's world have created an arena of contest, congestion, and competition among other space-faring nations [2]. Approximately 60 nations as well as a multitude of commercial and academic satellite operators currently work with thousands of space assets in Earth orbits [3]. The 1974 United Nations (UN) Convention on Registration requires nations launching objects into space to register basic orbit parameters and general spacecraft function [4]. Despite providing a symbolic step forward in international cooperation with regards to the space domain, the required basic orbit parameters provide little information necessary for accurate and real-time orbit determination for the growing list of active spacecraft in Earth orbits. In the years since the UN convention, the U.S. Air Force (USAF) has conducted its own mission to provide precise tracking of objects in space for its own assets as well as any other man-made object large enough to track [2].

The U.S. Department of Defense (DoD) and the USAF emphasize continued research of space situational awareness (SSA) to protect the US and allied space capabilities from an increasingly congested space environment [3]. From the Joint

Space Operations Center (JSpOC) and the dedicated set of ground radar and electro-optical (EO) sites around the globe that make up the Space Surveillance Network (SSN), the DoD actively tracks approximately 22,000 objects in Earth orbits [2]. Current research throughout the USAF focuses on improving the precise predictions of man-made spacecraft and debris with the primary objective of collision avoidance [5], but extended efforts must be taken to perform accurate orbit determination of additional objects in space due to the high level of uncertainty in the space environment. JSpOC requires constant improvement in SSA algorithms in order to support the U.S.'s increasingly important mission of protecting its space assets [6].

National security concerns limit international cooperation with respect to the current orbits and future maneuver plans of space assets [7]. Without the open source sharing of precise orbital information or plans to maneuver space assets, the U.S. and other space-faring nations face an increased risk for spacecraft collisions. As seen with the 2009 collision of the commercial communications satellite Iridium 33 and the decommissioned Russian military communications satellite Cosmos 2251, collisions in space can easily turn two highly capable assets into thousands of pieces of orbital debris. JSpOC uses a collection of astrodynamic algorithms standardized by Air Force Space Command (AFSPC) and assessed by the National Research Council (NRC) to track and estimate the location of objects in space and provide collision warning to any spacecraft at risk [2].

Much of the SSA effort is used to associate ground-based sensor readings with specific items in the space catalog [2]. When a spacecraft performs an unannounced maneuver, the errors in sensor measurements become greater than the required confidence interval of the cataloged object and its original orbit, creating an uncorrelated target (UCT) in the JSpOC database [2]. More research is needed to

2

improve tracking, prediction, and estimation of non-cooperative spacecraft that perform unknown maneuvers at unknown times to increase target correlation and the overall SSA mission [3].

1.2   Problem

This study assesses the detection and characterization of non-cooperative spacecraft maneuvers with space-based sensors in rendezvous and proximity operations (RPO) using adaptive estimation techniques. Previous research by Goff et al. demonstrated the ability to detect and track unknown maneuvers of non-cooperative spacecraft using ground-based radars [7]. Although adaptive estimation techniques have claimed to be more effective at detecting and tracking unknown maneuvers than traditional orbital estimation techniques [8], Goff admits that future work is necessary to evaluate scenarios where a spacecraft maneuvers into an area not covered by ground-based radars. The current research applies an estimation architecture similar to that in [8] using space-based sensors for spacecraft in geosynchronous orbit (GEO), filling in the limitations of ground-based sensors.

The motivation of this research identifies three potential interests for the operational use of adaptive estimation techniques for maneuver detection and characterization. Serving as the single most up-to-date space object tracking system, JSpOC needs an accurate and robust orbit determination network. Consistent detection and tracking of orbital maneuvers will improve JSpOC's ability to provide early warning prediction of satellite collisions. Detecting maneuvers of non-cooperative spacecraft will also provide insight to the commercial space industry, improving the state-of-the-art in orbital estimation for on-orbit rendezvous and servicing missions. This research also provides an assessment on applications of space-based assets to the maneuver detection problem, which will provide valuable

information to the USAF space acquisition community when applying adaptive estimation algorithms to future operational space missions. The overall research objectives of this study are tailored with these interests in mind to provide a clear path forward in terms of future operational applications.

The study is divided into three research questions focused on examining current adaptive estimation techniques and applications to relative satellite motion and proximity operations as well as assessing the performance of an adaptive estimation algorithm through a realistic parameter study. The following research questions shall be answered by the conclusion of this study:

- Can adaptive estimation techniques be applied to detect and characterize non-cooperative spacecraft maneuvers in satellite close proximity operations?

- How do sensor source and type, data rate, maneuver magnitudes, and relative trajectory affect the performance of an adaptive estimation algorithm?

- For what types of scenarios does an adaptive estimation algorithm fail to detect a maneuver or fail to characterize an accurate maneuver magnitude?

1.3 Document Overview

This document consists of five chapters, the first of which is an introduction to the motivation behind this study and its research objectives. Chapter 2 is a comprehensive literature review on the background, theory, and methodology behind this research, to include previous research done on statistical orbit determination (SOD), adaptive estimation, relative satellite motion, and space-based sensor analysis. Chapter 3 describes the methodology used in this study, presenting all of the necessary algorithms and equations discussed in Chapter 2 that will form the foundation for the variety of maneuver detection and characterization scenarios

necessary to accurately validate the different adaptive estimation algorithms used in this study. Chapter 4 contains the results and analysis of each maneuver detection and characterization scenario along with discussions assessing efficacy, timeliness of convergence, and comparisons to traditional estimation algorithms. This document concludes with Chapter 5, which summarizes the study and emphasizes the significance of the research while providing recommendations for future work.

II. Literature Review

The task of detecting maneuvers of non-cooperative spacecraft using adaptive estimation for RPO scenarios requires an extensive research effort in the areas of orbit determination, estimation theory, and relative satellite motion. This chapter reviews relevant literature that provides the groundwork for each topic of interest, including the derivations of notable equations and algorithms where necessary. This chapter also emphasizes previous research done in the area of spacecraft maneuver detection, providing realistic applications of current research into the overall topic of orbital estimation and tracking.

2.1   Statistical Orbit Determination

SOD is the generalized term used to describe the application of estimation theory and how to account for errors in observation measurements and uncertainties in the dynamics for orbit determination. SOD utilizes the principles of estimation theory through minimizing residual errors while predicting a spacecraft's orbital trajectory, often referred to as the states of the system. The principle of a minimum mean square error (MMSE) estimation algorithm is to take a series of dependent variables or measurements and produce an approximation of the state variables as well as a mean squared estimate for the error in each state. In satellite dynamics, the mean square error estimate produced is represented by the covariance matrix, which Wiesel defines as the correlation of the error estimate between each state variable [9]. The following sections supply the theory and basic derivations of each estimation technique used in this study and their current applications to SOD and the overall USAF SSA mission.

2.1.1 Applications of Estimation Theory

Originally developed by Carl Friedrich Gauss in the early 1800s, estimation theory uses statistics to estimate the error in a measured variable and correlate the estimate to a confidence factor for the measured variable. Gauss revolutionized the field of orbit determination by focusing on minimizing measurement and calculation errors instead of attempting to find the perfect dynamical equation to represent orbital motion [10]. Over a century later, the advancement of technology brought forth new estimation algorithms that take advantage of increasing computational speed and accuracy. Today, the USAF utilizes modern estimation theory to minimize observation errors when tracking space objects [2]. Tapley et al. provides an in-depth analysis at the estimation theory behind SOD and presents a realistic approach to building an orbit determination problem through defined orbital dynamics and initializing error and covariance estimates [11]. Before discussing the theory behind the estimation techniques used in this study, the estimation problem is defined in terms of the inherent error in a dynamical system as well as the states that define the system.

Gauss made the assumption that there is no perfect equation to describe the motion of a system, establishing the need for deterministic estimation theory. Modern estimation theory makes a second assumption in that there are no perfect measurements to determine the states of a system, requiring the need for stochastic estimation theory [9]. Through his founding of probability theory, Gauss defined imperfections in dynamical systems as random processes, otherwise known as noise [10]. For most dynamical systems, the noise in a state estimate can be defined by a normally distributed probability density function, also known as the Gaussian distribution as shown in Figure 1. Although noise is defined to be a random process, the assumption that the noise of the error is normally distributed is not only proven

by the central limit theorem but is also observed in the real world all the time. A complete proof of the central limit theorem can be found in [9].
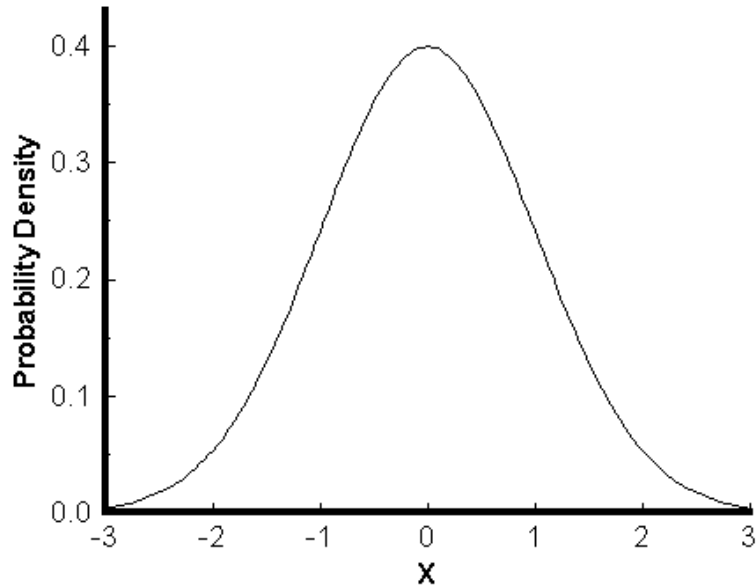
Figure 1. The Gaussian zero-mean probability density function

A state estimate described by Gaussian white noise is fully defined by a mean of the state, E(x), and a standard deviation of the state, σ_x. A dataset defined by a Gaussian distribution implies that approximately 99% of the points in the dataset are within 3σ of the mean of the set. Using Figure 1 as an example, E(x) = 0 and $\sigma_x = 1$. Unless otherwise stated, all instances of error in the dynamical and measurement equations of this study are assumed to be zero-mean, independent, white Gaussian noise. These assumptions for the current study imply that every state estimate has a normally distributed error centered about its mean, and each state error is uncorrelated with any other state error. Noise and errors in the system are further defined for this study in Chapter 3.

General applications of estimation theory for dynamical systems are built to estimate states that are related in some way to the variable dynamics of the system,

represented by the equations of motion. Wiesel defines a general state vector $\mathbf{x}$, which defines the states of the system [9]. The system is defined in Equation (2.1) by a series of differential equations that relate the changes of the state vector over time, denoted by the generalized function $\boldsymbol{f}$, and the confidence in the dynamical model, denoted by the random process $\mathbf{w}(\mathrm{t})$

$$\frac{d\mathbf{x}}{dt} = f(\mathbf{x}, t) + \mathbf{w}(t). \tag{2.1}$$

Another way to represent the dynamics is through a state transition matrix. The state transition matrix relates a previous state vector to a new state vector separated by some dependent variable, in this case a discrete time step $(t_2 - t_1)$. Shown in Equation (2.2), Stengel and other textbooks on estimation theory use the state transition matrix to define a discrete-time system with process noise [11, 12]

$$\mathbf{x}(t_2) = \boldsymbol{\Phi}(t_2, t_1)\mathbf{x}(t_1) + \mathbf{w}(t_1) \tag{2.2}$$

where $\boldsymbol{\Phi}(t_2, t_1)$ is defined as the state transition matrix, which for nonlinear systems can vary over each update of the state vector. The term for process noise, $\mathbf{w}(t_1)$, is considered a disturbance input for the system, and is still assumed to be white Gaussian noise.

Estimation theory also defines the relationship between the measurements and the state vector, along with the uncertainties associated with the measurements [12]. The measurement vector, $\mathbf{z}(t)$, is defined in Equation (2.3)

$$\mathbf{z}(t) = \mathbf{y}(t) + \mathbf{v}(t) = \mathbf{h}[\mathbf{x}(t)] + \mathbf{v}(t). \tag{2.3}$$

Stengel uses the output vector, $\mathbf{y}(t)$, to relate the state vector, $\mathbf{x}(t)$, to the measurement vector, $\mathbf{z}(t)$ with the measurement error represented by a noise

component, $\mathbf{v}(t)$ [12]. The output vector can be any combination of the states that the user has interest in, which is defined by the measurement basis function, $\mathbf{h}[\mathrm{x}(t)]$ [13].

In most cases, it is simple and efficient to define the state vector $\mathbf{x}$ as the position and velocity vector when dealing with particle dynamics. However, it can be useful and at times necessary to include other pieces of information regarding the dynamics of the system in the state vector such as coordinate transformations or osculating orbital elements. As long as the equations of motion can be defined with respect to the state vector, estimation theory can be used to track the changes to the state vector and the errors in the estimate of each state in the system.

2.1.2 Least Squares Estimation

Least squares estimation can be traced back to the original foundations of estimation theory [10]. By using the probability assumptions described in section 2.1.1, Gauss invented the least squares method to obtain orbits on objects with a limited amount of observations [9]. The main principle of deterministic least squares is to calculate the estimate state, $\hat{x}$, such that the square of the residuals is minimized. The calculation of the residuals, $\bar{\mathbf{r}}$, shown in Equation (2.4), is usually defined as the difference between the observed measurements and the predicted measurements, described earlier in Section 2.1 as the measurement vector and a function of the state vector [14]. A full derivation of both the linear and nonlinear least squares algorithm can be found in Vallado's text [15].

$$\bar{\mathbf{r}} = \mathbf{z}(t) - \hat{\mathbf{y}}(t) = \mathbf{z}(t) - \mathbf{h}[\hat{\mathbf{x}}(t)] \tag{2.4}$$

Although the least squares algorithm is effective in minimizing the residual error of the system, problems arise with SOD applications in terms of both

10

computational time and accuracy. Every observation available is incorporated into the least squares algorithm, and the state vector is sized on the order of the number of measurements. When these measurements are limited, as in the case of Gauss estimating the orbit of the asteroid Ceres [9], the least squares solution computed by hand is precise. Over the course of observing a satellite in low Earth orbit (LEO), however, an increasing number of measurements over time causes the memory requirements on a program to become significant.

Since the dynamics of an orbit are inherently nonlinear, the forces affecting the spacecraft at one observation could differ greatly from the forces at another observation over the course of many orbits around the Earth. This causes problems in the least squares solution, as the dynamical state model cannot be easily changed in real-time [14]. As the external forces on a satellite in orbit, such as aerodrag or the effects of J_2, grow increasingly nonlinear, treating older measurements with the same confidence as newer observations will cause significant errors in the least square solution [14].

One of the ways to solve the computational time and accuracy issues with the least squares algorithm is through batch processing. The main idea behind the batch least squares (BLS) algorithm is to continuously solve the least squares problem with available data without having to continuously calculate old data. Vallado provides the framework for solving the least squares problem through batch processing [15], while Tapley et al. steps through the derivation and application of the BLS algorithm [11]. This still produces a linearized solution to the nonlinear problem, so iterating may not converge on a minimized residual solution [15].

The BLS algorithm is a widely used technique for SOD because it is designed to handle a small number of observations over a significant period of time while still minimizing the error between the measurements and the state estimate. Since the

SSN ground radar system is tasked with tracking tens of thousands of space objects daily, the JSpOC orbit tracking and SSA missions are a useful application of the BLS algorithm [2]. Batch processing is used in these instances of SOD, which can take a series of observations over significant periods of time and fit the data to the predicted orbit while minimizing the residuals. Although the BLS technique is useful for a multitude of ground measurements spread out over many orbital periods, problems arise when system perturbations are not entirely known and are therefore modeled incompletely [16]. Due to the real-time requirements inherent in the maneuver detection problem analyzed in the current study, more sequential estimation methods are required over the BLS algorithm.

2.1.3   Kalman Filtering

A major issue with the least squares estimation technique is that the converged state and covariance matrix are based on a large batch of data that may have accumulated error over a prolonged period of time. No matter how accurate the estimate is, the least squares algorithm is always based on an epoch time and may not have a precise estimate for any state at a future epoch time. The solution to these inherent problems is sequential estimation, or computing the best state estimate of a time-varying process [15]. The Kalman filter (KF) solves the same least squares problem as BLS, but tries to minimize errors through sequential estimation [17].

Vallado cites two major differences between the least squares technique and the KF [15]. First, the KF continuously updates the epoch time, only predicting the state estimate at a future observation time. Second, the KF keeps all past information in the current estimate and covariance matrix, eliminating the need to continuously recalculate any past states or measurements at each time step.

The dynamical equations of motion as well as the measurement equations for orbit mechanics are often nonlinear in nature, and the linear KF is not always applicable. Therefore, the extended Kalman filter (EKF) is sometimes necessary [15]. Wright explains that the EKF is more dynamic than the BLS and is more ideal for orbit determination [18]. The EKF has a similar algorithm as the linear KF, but uses a Taylor series approximation at each time step in the propagation to temporarily linearize the dynamics and apply the optimal least squares solution.

Derivations of the linear KF and EKF can be found in many astrodynamics and estimation textbooks [9, 11, 12] as well as other works utilizing sequential estimation [13, 19]. Both the KF and the EKF start with an initial guess of the state and covariance matrix

$$\hat{\mathbf{x}}(t_0) = \hat{\mathbf{x}}_0$$
$$\mathbf{P}(t_0) = \mathbf{P}_0.$$

$$(2.5)$$

Using Equations (2.2) and (2.3) to define the state and measurement equations, the process and measurement noise are assumed to be independent, zero mean, normal probability distributions, with covariances shown in Equation (2.6)

$$p(w) \sim N(0, \mathbf{Q})$$
$$p(v) \sim N(0, \mathbf{R})$$

$$(2.6)$$

where the process noise covariance , $\mathbf{Q}$, and the measurement noise covariance, $\mathbf{R}$, are free to change at each time step to represent the confidence in the dynamics or the data at any time during the propagation of the filter.

The first step in the KF is to propagate the state vector from $\mathbf{x}_{k-1}$ to $\mathbf{x}_k$ depending on the dynamical equation of the system. The covariance matrix is also propagated from $\mathbf{P}_{k-1}$ to $\mathbf{P}_k$ based on the mean squared error of the predicted state. The predicted state, $\mathbf{x}_k$, is then corrected by a combination of the measurement basis function, $\mathbf{h}_k[\mathbf{x}_k^-]$, the predicted state covariance matrix, $\mathbf{P}_k^-$, and the measurement covariance matrix, $\mathbf{R}_k$. The correction calculation shown in equation 2.7 is called the Kalman gain. In both the KF and EKF algorithms, the Kalman gain is calculated by the same equation

$$\mathbf{K}_k = \mathbf{P}_k^- \mathbf{H}_k^T (\mathbf{H}_k \mathbf{P}_k^- \mathbf{H}_k^T + \mathbf{R}_k)^{-1} \tag{2.7}$$

where the matrix $\mathbf{H}_k$ is a linear measurement basis function multiplied by $\hat{\mathbf{x}}_k^-$ to get the output vector, $\mathbf{y}$. In Equation (2.7), the $^-$ superscript represents the previous predicted estimate in the algorithm, while the updated state and covariance estimate shown in Equation (2.8) is represented by the $^+$ superscript. The state and covariance estimate are updated using the same equations for the linear and nonlinear case.

$$\hat{\mathbf{x}}_k^+ = \hat{\mathbf{x}}_k^- + \mathbf{K}_k(\mathbf{z}_k - \mathbf{H}_k \hat{\mathbf{x}}_k^-) \tag{2.8a}$$

$$\mathbf{P}_k^+ = (\mathbf{I} - \mathbf{K}_k \mathbf{h}_k[\hat{\mathbf{x}}_k^-])\mathbf{P}_k^- \tag{2.8b}$$

Notice that the last term in Equation (2.8a) is the residual vector defined in Equation (2.4), only this time it only represents the residual vector at the specific time step instead of at every measurement for the least squares algorithm.

Looking back at Equations (2.5) to (2.8b), it would seem that the linear KF and the EKF follow the exact same algorithm, which during the

14

prediction-correction stage of the algorithm is completely true. The primary difference between the KF and the EKF is that the EKF must linearize its dynamics and measurement basis function in order to propagate in discrete time. If the dynamics follow the generalized functions shown in Equation (2.1) and (2.3), then the state estimate is propagated by Equation (2.9), and the linearized measurement basis function is shown in Equation (2.10).

$$\mathbf{x}_k = \int_{t_{k-1}}^{t_k} \left[\dot{\mathbf{x}}_{k-1}\right] dx + \mathbf{x}_{k-1} \tag{2.9}$$

$$\mathbf{H}_k = \frac{\partial \mathbf{z}}{\partial \mathbf{x}_k^-} \tag{2.10}$$

Using a linearized form of the dynamics and the measurements at each time step, the EKF can easily transform the nonlinear dynamic systems seen in orbit mechanics into a simplified model that can be propagated through the KF algorithm. However, no matter how small the time step, any linearized model of nonlinear dynamics are bound to have inherent errors, which can be unacceptable for SOD.

2.1.4 The Unscented Kalman Filter

Accuracy concerns arise with the EKF because the algorithm must differentiate the measurement and dynamic functions with respect to the state vector in order to linearize the problem at every time step. Julier and Uhlmann developed a nonlinear Kalman filter called the unscented Kalman filter (UKF) for improved performance and accuracy [20]. While the EKF simply linearizes the dynamics of the system through each step in the estimation, the UKF overcomes the difficulties that arise from linearization by propagating the mean and covariance of the state vector

15

through nonlinear transformations [21] . Instead of relying on numerical integration or linearized propagation, the UKF moves a weighted distribution of critical points based on the current estimate of the covariance matrix. The weighting methods used in this study for the nonlinear unscented transformation (UT) are outlined in Section 3.2.1.

As explained in Teixeira et al., the UKF is similar in computational efficiency and superior in accuracy to the EKF when implemented properly for orbit determination [22]. In addition, Teixeira et al. conclude that the UKF is able to converge uniformly better than the EKF for time-sparse measurements [22]. Pardal et al. also show that the UKF outperforms other filters when observations are less frequent, specifically testing this hypothesis with pseudo range observations [23].

2.1.5   Filter Smoothers

At the end of each scenario, a backwards smoother applied to the filter can further improve the estimated state. Wright and Woodburn explore different combinations of fixed epoch smoothers (FES) with an EKF to improve state estimates [24]. The FES is ideal for discrete satellite observations used in orbit estimation; new measurements processed through the EKF in real-time are also used to recursively update the estimated state and covariance at some previous epoch time. Helmick et al. examines a fixed-interval smoothing algorithm using an adaptive estimation framework, which updates all estimates within an interval from the current estimate [25]. This approach can be costly for orbit estimation in real-time because the algorithm requires n^2 smoothers working in parallel for every n models.

Another type of smoother developed for the UKF by Särkkä is the unscented Rauch-Tung-Striebel smoother [26]. Instead of combining the results of a forward

running UKF for the backward-working algorithm, a backward smoother is used to calculate suitable corrections to the forward algorithm. This concept can improve the state error for scenarios with large nonlinearities and unknown dynamics such as a maneuver because it can update previously erroneous state estimates with newly propagated dynamics. However, because these smoothing algorithms require varying levels of post-processing, they are not ideal for real-time estimation scenarios and will not be tested in this study.

2.2   Multiple Model Adaptive Estimation

The NRC has expressed the need for considering future research in multiple model adaptive estimation (MMAE) with regards to the SSA mission and more specifically maneuver detection [2]. Tracking a non-cooperative spacecraft and detecting unknown maneuvers requires an adaptive estimation technique because the noise components of the non-cooperative spacecraft are unknown and must be estimated. Magill outlines the fundamentals of adaptive estimation and its applicable derivations [27]. MMAE uses a bank of KFs that all make different assumptions about the dynamics of the system, specifically in the covariance of the process noise, $\mathbf{Q}$.

The adaptive framework allows for different ways to account for unexpected changes in the state or covariance estimates. Each of the filters has a series of weighting coefficients that can change based on algorithm specific rules regarding calculations and filter initializations. Li et al. presents an adaptive filter using a series of UKFs to approximate and adjust the process noise covariance throughout the propagation of the algorithm [28]. Moose developed an adaptive state estimator for the general maneuvering target problem and concluded that the adaptive estimator with a band of KFs is certainly superior to the linear KF [29]. Although

proven accurate in estimating uncertainties in the dynamics of the target, the adaptive estimation technique still must make a series initial guesses on the process noise covariance matrix. Without interaction, the MMAE could still diverge if the guesses of the process noise covariances are not accurate.

2.2.1 Interacting Multiple Models

The concept of interacting multiple models (IMM) is used to solve the problem of poor initial guesses in the adaptive estimation algorithm. Li et al. states that the IMM method is the prevailing approach to modern maneuvering target tracking [30]. The IMM combines the inputs of several models at each time step and uses the statistics of the residuals to weigh the impact of each model at each step. Compared to the general adaptive estimation method, the IMM algorithm creates a probability density function (PDF) of the model weights, which produces the converged results as a combination of multiple models that could be the correct covariance estimate. The specific IMM algorithm and PDF used in this study are outlined in Section 3.2.3.

When applying general MMAE techniques to filter through unknown maneuvers, covariance inflation must occur to prevent divergence [31]. Covariance inflation is the process of assuming no confidence in the dynamical model during the maneuver so that the measurement basis function can dominate the state estimate [11]. Through covariance inflation, however, a trade off occurs. A large covariance causes a high probability of convergence, but also a high chance for errors in the state estimate. The IMM filter prevents the need for determining optimal covariance sizes that are only valid for specific dynamical systems by providing a method to mix different covariance estimates and weighting the results based on the likelihood probability calculated for each model [32]. For this reason, the IMM method is

considered suboptimal because it may not converge on the exact covariance for the target orbit during maneuver detection, but as Goff shows in [7], the IMM method is effective in maneuver detection algorithms when limited information is known about non-cooperative spacecraft maneuvers.

The IMM framework steps closer towards being able to handle the maneuver detection problem in that it accounts for the uncertainty in the dynamics of the non-cooperative spacecraft unknown to the observer through adaptive covariance analysis. However, large changes in the dynamics, such as an unknown active thrust maneuver at an unknown time, cannot be accounted for simply through covariance inflation and adaptive estimation.

2.2.2 Variable State Dimension Filter

The variable state dimension (VSD) filter is a solution to handling major unknown changes in the dynamics of a maneuvering spacecraft. Bar-Shalom et al. was the first to apply a variable dimension filter to a general maneuver tracking scenario [33]. The VSD filter is optimal for dealing with unknown maneuvers because the filter has the ability to add or subtract states based on the deviation of the estimated state from the measured state, defined earlier as the residual vector. High residuals are potentially caused by a fundamental error in the equations of motion of the system, but a VSD that monitors residuals could account for errors by adding additional states to the state vector (such as a thrust vector) for a spacecraft changing its dynamics by maneuvering.

Bar-Shalom et al. expand the algorithm of the VSD filter in their text [34]. The fundamentals of the VSD filter can be structured as any KF previously discussed in Section 2.1.3. In this case, two filter models are used: the quiescent model, with states defined as the position and velocity vector of the target, and the maneuvering

model, which tracks an acceleration vector as additional states to the system. The model switching indicator uses a fading memory average of the sequentially calculated residuals of the filter based on the quiescent model, seen in Equation (2.11)

$$\Psi_k = \bar{\mathbf{r}}^T \mathbf{S}_k^{-1} \bar{\mathbf{r}} \tag{2.11}$$

where $\mathbf{S}_k$ is the covariance matrix of the residual vector, also known as the measurement covariance. The scalar value defined in Equation (2.11) is known as the Mahalanobis distance (MD), and is referred to as the maneuver detection statistic in the current study. Compared to the commonly used Euclidean distance (ED), the MD takes into account the correlation in the data through the measurement covariance matrix [35], which allows the estimation algorithm to converge on a minimized set of residuals without detecting a false maneuver.

The MD value is based on a chi-square distribution, and the maneuver threshold used to detect the maneuver start and stop times is based on a two-sided test at a significant level $\alpha = 0.0005$, which corresponds to a probability of p = 0.999 that the maneuver detection statistic is less than the critical value. Equation (2.12) shows the chi-square distribution PDF:

$$\text{PDF}(x; k) = \frac{x^{k/2-1} e^{-x/2}}{2^{k/2} \Gamma\left(\frac{k}{2}\right)}. \tag{2.12}$$

Here x is the maneuver detection statistic, k is the degrees of freedom for the system, and Γ denotes the gamma function. Table 1 shows the critical values of a chi-square distribution based on the degrees of freedom for the system. Based on the critical values for the 4 and 6 degrees of freedom for the states of the system

defined in this study, the maneuver threshold is maintained at a constant value of 20 throughout the maneuver detection scenarios.

Table 1. Critical values of a chi-square distribution

DOF	Critical Value for p = 0.999
1	10.828
2	13.816
3	16.266
4	18.467
5	20.515
6	22.458

Because the change in the residual vector over the observation time varies depending on the dynamics of the target, the VSD algorithm assumes that the maneuver started before the VSD detects the maneuver. Bar-Shalom et al. define the effective window length of detecting a maneuver as the multiplicative sum of a weighting value, α, as the discrete time counter, k, approaches infinity [34]. Since the weighting value is defined between $0 < \alpha < 1$, the effective window length, Δ_α, for detecting a maneuver is described in Equation (2.13).

$$\Delta_\alpha = \frac{1}{1 - \alpha} \qquad (2.13)$$

Although Bar-Shalom concludes that this metric is an acceptable window to backtrack through the data and estimate the start of the maneuver, there is no metric in defining the weighting matrix α besides the intuitive confidence in the past measurements. A low α constitutes a low confidence in the previous residual vectors in the filter, and Equation (2.13) therefore assumes the maneuver started earlier than if there was a higher confidence in the previous estimates. Figure 2

shows the transition of estimating using the quiescent model to estimating using the maneuvering model using the detection criteria outlined by Bar-Shalom et al. [33]. Although not explicitly stated, the metric for detecting the end of the maneuver is also calculated using the same algorithm that detects the start of the maneuver.
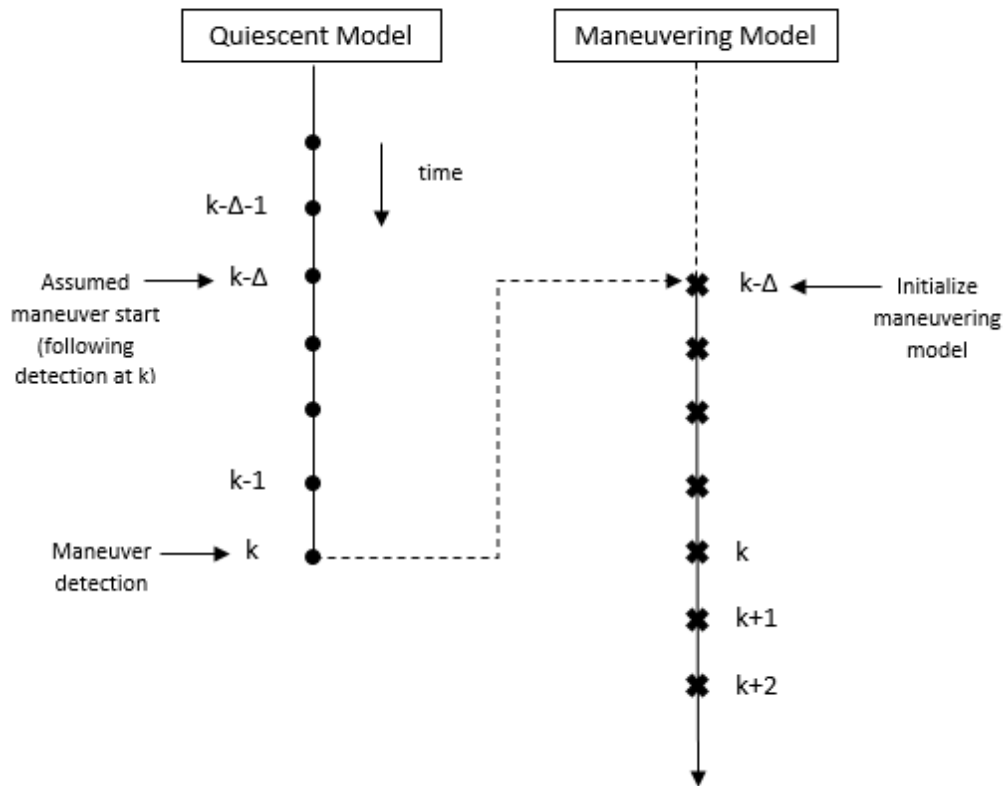
Figure 2. VSD filter switching from quiescent model to maneuvering model

Using the extensive review of estimation theory shown in Section 2.1, this study uses the background shown in Section 2.2 to develop the algorithm necessary to detect unknown maneuvers of non-cooperative spacecraft using an observer satellite collecting measurements in close proximity. Specifics regarding the adaptive estimation techniques used in the current study are presented in Chapter 3. The

following sections review the necessary background, theory, and equations necessary to describe the motion of spacecraft flying relative to each other in Earth orbits.

2.3 Relative Satellite Motion

As stated in Section 1.2, this study applies adaptive estimation techniques discussed in Section 2.2 to RPO scenarios with the objective of non-cooperative maneuver detection and characterization. The differential equations established in Equation (2.1) for any estimation algorithm must be able to accurately describe the dynamics of satellites relative to each other. Relative satellite motion provides a convenient and efficient method to define the dynamics of RPO spacecraft without the need for an inertial reference frame.

For every scenario described in this study, consider two satellites in Earth orbits, one identified as the "chief" and the other identified as the "deputy". For the purposes of consistency, the chief in this study is also considered the "observer", or the spacecraft taking measurements on the deputy, which will be considered the "target". When deriving the equations of motion for RPO scenarios, a new non-inertial coordinate frame must also be considered to describe the orbit of the target with respect to the observer.

2.3.1 Local-Vertical Local-Horizontal Reference Frame

As with all dynamical systems, the reference frame used to describe satellite motion is just as important as the equations of motion themselves. The reference frame most often used to describe relative satellite motion is the local-vertical local-horizontal (LVLH) frame, also called the Hill frame for his original derivation in describing the Moon's orbit around Earth with respect to the Sun [36]. The origin of the LVLH frame is centered at the chief, with the x-axis pointing in the

direction of the chief's position vector with respect to the Earth, the z-axis pointing

normal to the orbital plane, and the y-axis completing the right handed coordinate

system. The y-axis is generally pointed in the along-track direction, and if the

chief's orbit is circular then the y-axis is directly aligned with the chief's velocity

vector. Figure 3 shows the LVLH reference frame centered at the chief spacecraft,

providing a visual relationship between the states $[x,y,\dot{x},\dot{y}]$ and the space-based

sensor measurements range (ρ), range rate $(\dot{\rho})$, and azimuth (α). Further discussion

regarding space-based measurements can be found in Section 2.4.1.
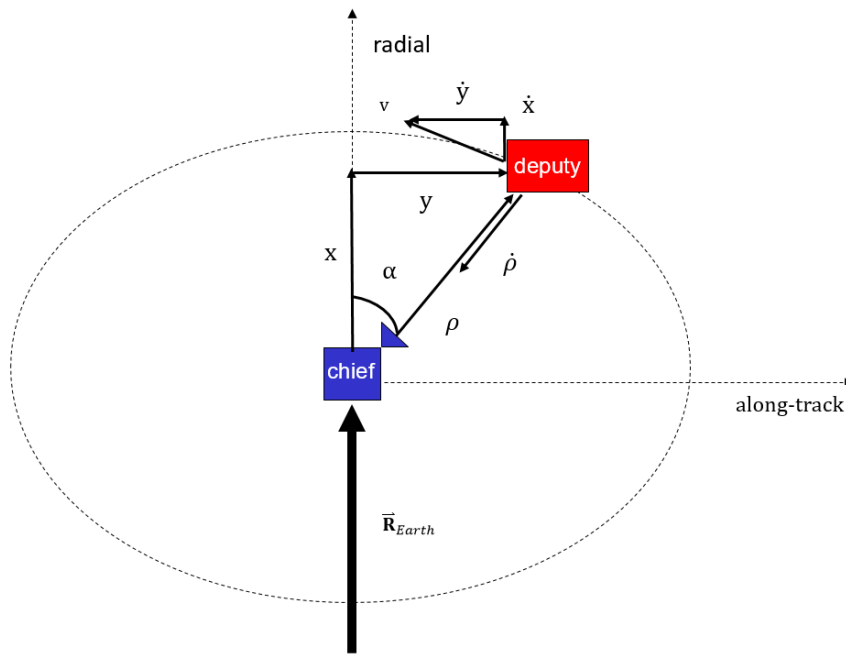
Figure 3. The LVLH reference frame

2.3.2   The Hill Clohessy Wiltshire Model

The Hill Clohessy Wiltshire (HCW) model is the most widely used set of

equations that accurately describe the relative motion of two spacecraft operating in

close proximity. The equations of motion were originally developed by Clohessy and

Wiltshire in 1960 for satellite rendezvous [37] and are similar to Hill's equations of

24

motion in his lunar theory [36]. Derivations of the HCW equations can be found in many astrodynamic textbooks [16, 38, 39]. The full nonlinear equations of relative motion are shown in Equation (2.14)

$$\ddot{x} - 2n\dot{y} - \dot{n}y - n^2x - \frac{\mu}{r^2} = \frac{-\mu}{r_d^3}(r + x) + f_x \tag{2.14a}$$

$$\ddot{y} + 2n\dot{x} + \dot{n}x - n^2y = \frac{-\mu}{r_d^3}y + f_y \tag{2.14b}$$

$$\ddot{z} = \frac{-\mu}{r_d^3}z + f_z \tag{2.14c}$$

where x, y, and z are the position components; $\dot{x}$ and $\dot{y}$ are the velocity components; and $\ddot{x}$, $\ddot{y}$, and $\ddot{z}$ are the acceleration components of the target in the LVLH frame. The variable r and r_d refer to the distance of the chief and deputy with respect to the Earth, the variables n and $\dot{n}$ refer to the mean motion of the chief and its first time derivative, and the variable μ refers to the gravitational constant of the Earth.

The full nonlinear equations of motion are difficult and time consuming to propagate, and the estimation algorithms presented in Section 2.1 are designed to handle small unknown errors in the dynamics, which allows for some simplifying assumptions. The three major assumptions that allow for the full linearized model of the HCW equations are that the two spacecraft are in Keplerian motion, so the only force modeled is Earth's gravitational field as a point mass; the chief is in a circular orbit, so its mean motion is assumed constant; and the distance between the satellites is small compared to their orbital radii, so $r_d \approx r$. For many formation flying missions in a near-circular orbit and with proper estimation techniques, these assumptions tend to be valid [13, 40]. The simplified HCW equations are shown in Equation (2.15):

$$\ddot{x} - 2n\dot{y} - 3n^2 x = f_x \tag{2.15a}$$

$$\ddot{y} + 2n\dot{x} = f_y \tag{2.15b}$$

$$\ddot{z} + n^2 z = f_z. \tag{2.15c}$$

These equations are written in the LVLH reference frame, where x, y, and z are used to describe the deputy's position with respect to the chief in the radial, along-track, and cross-track directions, respectively. The term n in Equation (2.15) is used to denote the mean motion of the chief, which can be found using the Earth's gravitational constant, μ, and the semi-major axis of the chief, a_c, as seen in Equation (2.16)

$$n = \sqrt{\frac{\mu}{a_c^3}}. \tag{2.16}$$

In this study, another simplified nonlinear form of the HCW equations is explored. The assumptions of Keplerian motion and a circular chief are still valid, but removing the relative distance assumption allows for scenarios with significant distances between the chief and the deputy without losing accuracy. The nonlinear HCW equations without the relative distance assumption are shown in Equation (2.17).

$$\ddot{x} - 2n\dot{y} - n^2 x - \frac{\mu}{r^2} = \frac{-\mu}{r_d^3}(r + x) + f_x \tag{2.17a}$$

$$\ddot{y} + 2n\dot{x} - n^2 y = \frac{-\mu}{r_d^3}y + f_y \tag{2.17b}$$

$$\ddot{z} = \frac{-\mu}{r_d^3}z + f_z \tag{2.17c}$$

26

The right-hand side of Equations (2.14), (2.15), and (2.17) allow for any external forces acting on the system to be added to the dynamics as a perceived relative acceleration on the system, which is used in this study as the acceleration force vector of the deputy when conducting maneuvers.

Assuming the linearized HCW equations of motion shown in Equation (2.15) have no external forces acting on the system, the analytical solution to the HCW equations is shown in Equation (2.18)

$$x = \frac{\dot{x}_0}{n} \sin(nt) - (3x_0 + \frac{\dot{y}_0}{n}) \cos(nt) + (4x_0 + \frac{2\dot{y}_0}{n}) \cos(nt) + (4x_0 + \frac{2\dot{y}_0}{n}) \quad \text{(2.18a)}$$

$$y = \frac{2\dot{x}_0}{n} \cos(nt) + (6x_0 + \frac{4\dot{y}_0}{n}) \sin(nt) - (6nx_0 + 3\dot{y}_0)t - \frac{2\dot{x}_0}{n} + y_0 \quad \text{(2.18b)}$$

$$z = \frac{\dot{z}_0}{n} \sin(nt) + z_0 \cos(nt) \quad \text{(2.18c)}$$

$$\dot{x} = \dot{x}_0 \cos(nt) + (3nx_0 + 2\dot{y}_0) \sin(nt) \quad \text{(2.18d)}$$

$$\dot{y} = -2\dot{x}_0 \sin(nt) + (6nx_0 + 4\dot{y}_0) \cos(nt) - (6nx_0 + 3\dot{y}_0) \quad \text{(2.18e)}$$

$$\dot{z} = \dot{z}_0 \cos(nt) - nz_0 \sin(nt) \quad \text{(2.18f)}$$

where x_0, y_0, etc. are the relative initial conditions of the deputy at some epoch time, t_0. From Equation (2.18e), HCW dynamical system experiences simple harmonic motion when the following constraint is met:

$$\dot{y}_0 = -2nx_0 \quad \text{(2.19)}$$

Using the constraint from Equation 2.19, the deputy spacecraft follows a stabilized 2x1 elliptical trajectory relative to the chief, referred to in other RPO works as natural motion circumnavigation (NMC) [41]. An NMC trajectory is a

convenient relative orbit that is used to create initial conditions for the scenarios presented in this research.

Using the equations of motion outlined in this section, the estimation algorithm developed in Chapter 3 is able to relate the current states of the system to the future states of the system in a way that is realistic to the relative satellite motion aspect of the study. Although there are major assumptions made to simplify the relative satellite equations of motion, using the process noise covariance analysis discussed in Section 2.2 can handle errors in the dynamics of the system while still using the simplifying assumptions in the algorithm. The final equations that are necessary to the estimation algorithm relate the measurements collected by the observer on the target to the relative orbital states of the target.

2.4   Space Sensor Analysis

Although the relative satellite motion dynamics defined in Section 2.3 use the coordinates x, y, and z in the LVLH frame to derive the equations of motion, the sensor measurements that are fed into the estimation algorithm do not directly measure position and velocity in LVLH frame coordinates. As mentioned in Section 1.2, this study analyzes an adaptive estimation algorithm against multiple types of measurements and measurement noise levels to make indications between algorithm performance and the quality of space-based sensors required. The types of measurements analyzed in this study are a combination of range-azimuth-elevation and range-range rate measurements.

2.4.1   Space-based Measurements

Escobal details several techniques for orbit determination using combinations of available data [42]. A common set of raw measurements obtained from a

space-based sensor is range, azimuth, and elevation, defined similarly to ground based measurements but here in the LVLH frame [13]:

$$\mathbf{z} = \mathbf{h}[\mathbf{x}(t)] = \begin{bmatrix} \rho \\ \alpha \\ \epsilon \end{bmatrix}_{LVLH} = \begin{bmatrix} \sqrt{x^2 + y^2 + z^2} \\ \arctan \frac{y}{x} \\ \arcsin \frac{z}{\rho}. \end{bmatrix} \tag{2.20}$$

Equation (2.20) is used as the nonlinear measurement basis function to relate the measurements back to the states of the problem. Another type of space-based sensor capability to be analyzed in this study is collecting measurements of range and range rate. This allows us to have some insight into not only the position of the deputy but also its velocity relative to the chief. The range and range-rate nonlinear measurement basis function is presented in Equation (2.21) [9]:

$$\mathbf{z} = \mathbf{h}[\mathbf{x}(t)] = \begin{bmatrix} \rho \\ \dot{\rho} \end{bmatrix} = \begin{bmatrix} \sqrt{x^2 + y^2 + z^2} \\ \frac{x\dot{x} + y\dot{y} + z\dot{z}}{\sqrt{x^2 + y^2 + z^2}} \end{bmatrix}. \tag{2.21}$$

2.4.2 Measurement Collection Techniques

A significant consideration when running estimation algorithms using space-based measurements outlined in Section 2.4.1 is the frequency of available and accurate sensor data. Much of this study assumes that sensor data is widely available on the observer looking at the target, but a space-based environment breeds a multitude of opportunities for large data errors, especially in non-cooperative scenarios.

Much of the previous literature on space-based observability analysis focuses on cooperative measurement collection for formation flying, but many measurement collection techniques can be applied to a non-cooperative scenario without any major fundamental technology upgrades. One of the most common approaches to

29

space-based SSA is the angles-only approach because it is useful at gathering measurements using solely vision-based navigation; Gaias discusses this approach in a non-cooperative setting using only a space-based camera [43]. Gaias enhances the accuracy of space-based servicing missions by converting angles-only data into relative orbital elements (ROEs). However, acquiring range data can be crucial when dealing with a target in close proximity to the observer, which requires more complex measurement collection techniques.

Junkins discusses vision-based navigation using a position sensing diode for RPO [44], but this requires targeting beacons to sense certain wavelengths of light, which is impossible in the non-cooperative scenario. Whittaker shows that space-based measurements can be acquired using a photometric sensor to correlate light intensity with range from the target [45]. Although this technique improves upon an angles-only approach, it requires reflected light from the Sun as well as sensor calibrations based on the material properties from the target spacecraft, which may not be available in a non-cooperative scenario. Krutz analyzes a radiometric sensor in a space-based mission to detect and track spacecraft debris [46]. Although this is an ideal non-cooperative scenario, Krutz admits that it would be difficult to categorize debris solely based on captured light intensity because a large debris far away would reflect the same amount of energy as a small debris closer to the observer. All of these EO sensors have inherent blind spots when the target spacecraft is in between the observer and the Sun, often referred to as the Sun vector. These EO sensors also require some form of cooperation in order to acquire accurate range data from the target.

The most common technique for collecting accurate range measurements without the need for cooperation is a light detection and ranging (LIDAR) sensor [47, 48]. A LIDAR sensor deploys a laser beam aimed at the target, and the sensor

measures the time it takes the reflected beam to return to the observer. Knowing that the beam travels at the speed of light, the distance traveled can be calculated by measuring the time traveled round trip between the target and the observer. The laser range finder is highly accurate because it does not experience atmospheric scattering in space, and its sensor bandpass is extremely narrow centered on the laser's nearly monochromatic wavelength. The effectiveness of a LIDAR device on a non-cooperative spacecraft lies in the reflectivity of the target's material at the laser's wavelength. However, with a narrow spectral bandwidth and a high powered laser, the sensor should still detect the laser light reflected off the target without a large gap in data caused by the Sun vector [48]. Once a range measurement is confirmed, the range rate measurement is collected by examining the Doppler effect of the reflected wavelength of the laser beam compared to the wavelength of the transmitted laser beam [49].

For the non-cooperative space-based RPO scenarios in this study, a realistic sensor suite for an observer collecting range, range rate, and angles data effectively would be a combination of EO and LIDAR sensors. In a realistic scenario, an EO sensor would sweep over a large area until the reflected light from the target generates relative angle measurements from the observer. As the angle measurements increased in accuracy, the LIDAR sensor would be able to effectively point and follow the target, collecting range and range rate data. This study assumes full measurement knowledge of the target in terms of range, range rate, and angles data, which implies the initial orbit determination (IOD) on the target is complete. Although this assumption is highly sensitive to the ability of the observer to collect accurate and abundant measurements, an in-depth observability analysis is not performed in this study and is left as future work.

2.4.3 Measurement Noise

One of the defining characteristics in assessing algorithm performance is measurement noise. Applying the current study to the USAF SSA mission requires accurate estimates in space-based sensor performance. Modern laser range finder technology developed by Hablani for applications in spacecraft relative navigation and rendezvous is used as a baseline for realistic assumptions regarding measurement accuracy and noise [47]. These measurement accuracy values are compared to previous literature on relative spacecraft estimation [13]. The measurement noise will be assumed constant throughout each individual scenario, but the process noise of the algorithm will be estimated by each filter continuously. Error and noise estimation is outlined in greater detail in Chapter 3.

2.5 Summary

This chapter conducted a review of past and current research efforts in the areas of orbit determination, estimation theory, adaptive estimation, and relative satellite motion. Background for the theory necessary to set up the maneuver detection problem was outlined. Basic derivations of the general equations used in this study were investigated and presented. Conclusions from the research completed on the current applications of adaptive estimation algorithms show that the scenarios developed in this study are unique and will provide a positive contribution to the areas of study reviewed in this chapter. Further development of the equations and algorithms used in this study, including specific applications to maneuver detection scenarios, are discussed in Chapter 3.

III. Methodology

This study focuses on investigating adaptive estimation techniques to detect and characterize spacecraft maneuvers given a set of space-based measurements. Section 1.2 lists the relevant research questions that will be addressed during this research. The following chapter outlines the specific procedures and algorithms to be used, how data will be collected through simulated scenarios, and what analysis criteria will imply success regarding the research questions defined in this study.

3.1   Research Questions Reviewed

The research questions answered by this study transform the complex problem of detecting non-cooperative maneuvers using adaptive estimation into a scoped and logical path forward. The research questions encompass all aspects of assessing a newly implemented algorithm, including efficacy, performance, and limitations. The first step before research can begin is to analyze the methodology behind how each research question can and will be answered to the fullest ability of this study.

The first research question addresses the first and foremost problem when assessing a new algorithm: efficacy. Does each IMM estimation algorithm work as anticipated, and what are specific requirements placed on each algorithm in order to guarantee success? For this first problem, realistic parameters in each maneuver detection scenario, such as availability of measurement data, will be adjusted for the sake of efficacy. Scenario parameters will continue to have fewer simplifying assumptions as the research progresses to assess performance and failure modes. The MMAE algorithm that detects a spacecraft maneuver for the simplest case is sufficient for completing the first research question, but success in the simplest case may not provide adequate data with regards to performance.

The second research question lists specific variables that will be used to assess the performance of each adaptive estimation algorithm. Sensor source relates to different types of measurement data available in an RPO scenario as well as realistic estimates for measurement noise to be implemented based on the current space-based sensor technology available. Hablani's patent for a space-based laser range finder has a convenient table for the expected level of noise in the output of the sensor [47], which will produce range, azimuth, and range rate data on the target satellite.

Maneuver magnitudes refers to the different types of space-based propulsion devices that produce many different levels of thrust. While a large solid rocket has the capability of inserting a satellite into a completely new orbit regime, other satellite missions utilize electric, cold gas, or liquid propellants for simple orbit maintenance or attitude determination. Table 2 lists a set of common propulsion systems used in orbit along with typical ranges for specific impulse and thrust [50].

Table 2. Common space-based propulsion systems and their applications

Propulsion System	Typical I_{sp} Range	Nominal Thrust	Common Applications
Cold Gas	45-73 s	0.05-3.5 N	orbital maintenance and maneuvering; attitude control
Solid	290-304 s	25-80 kN	orbit insertion
Liquid Monopropellant	200-235 s	1.5-445 N	orbital maintenance and maneuvering; attitude control
Liquid Bipropellant	274-467 s	0.1-100 kN	orbit insertion; orbital maintenance and maneuvering; attitude control
Electric	500-3,000 s	20-2,000 mN	orbit maintenance and maneuvering; attitude control

The data presented in Table 2 will provide a realistic set of maneuver magnitudes to be utilized in developing scenarios to test each adaptive estimation algorithm. Nominal thrust calculations for space-based propulsion systems are measured in Newtons, which allows the spacecraft user to calculate an applied force on the spacecraft. However, the dynamical equations used to propagate the estimation algorithms, as seen in Equation (2.15), are the second time derivative of the state vector, which conceptually is the acceleration of the target with respect to the observer. When estimating the thrust vector throughout each maneuver detection scenario, it is not in fact the applied force on the target spacecraft but the perceived acceleration of the target in the LVLH coordinate frame centered on the observer. Given mass and propulsion information about the target, an applied thrust could be derived from the maneuver magnitudes characterized in each scenario.

The third parameter that will be used for assessing algorithm performance is the relative trajectory of the target satellite. As stated in Section 2.3.2, the HCW equations of motion assume that the deputy satellite is relatively close to the chief satellite [37]. Although there is no explicit distance for divergence of the dynamics, the further away the deputy gets from the target the less accurate the dynamical model becomes. A large relative trajectory becomes a problem for the estimator because the process noise continues to grow as the confidence in the dynamics fades, until the point where the covariance of the process noise no longer accurately describes the standard deviation of the estimate from the dynamics [9].

Vallado notes that significant errors are presented for maneuver detection when using traditional least squares or filter techniques on orbital data because of a lack of dynamical knowledge during and post-maneuver [15]. Goff concludes that the MMAE algorithm outperforms all other traditional estimation routines by a factor

of 700 in maneuver detection scenarios over the course of just one orbit [7]. This study will assess these claims for the application of the adaptive algorithm using space-based maneuver detection scenarios.

Much of the data that assess the performance of the adaptive estimation algorithm also answers the third research question: at what point does the algorithm fail to converge on a solution? Many of these limitations are answered previously, such as the minimum thrust that is able to be detected accurately or the maximum distance away from the target where space-based measurements become unrealistic. Another area of performance considered for the third question is the availability of data for the observer. Through answering the first research question, the adaptive estimation algorithm will be proven valid with unlimited measurements on the target at all times throughout each scenario. This simplifying assumption is not only unchallenging but also unrealistic. Through answering the third research question, assessments will be made on the sparsity of the measurement data while still proving algorithm success.

3.2   Overview of the Approach

In order to sufficiently answer all parts of the research questions detailed in Section 3.1, an in-depth analysis on how the MMAE algorithm is used in this study must be conducted. Chapter 2 reviewed the background behind MMAE and the foundations of the VSD filter, but the specific design of the algorithm used in this study is presented here.

3.2.1   Kalman Filter Algorithms

As discussed in Sections 2.1.3 and 2.1.4, tracking a target in real-time with nonlinear measurements shown in Equations (2.20) and (2.21) requires a nonlinear

recursive estimation algorithm. The two estimation filters explored in this study are the EKF and the UKF. The systems are set up the same for both filters using Equations (2.1) and (2.3) to set up the state and output vector, Equations (2.15) and (2.17) to set up the relative satellite motion dynamics, and Equations (2.20) and (2.21) to set up the measurement basis function.

These equations discussed in depth in Chapter 2 are sufficient to initialize and propagate the EKF for the scenarios in this study, but some predefined weights are required for initializing the UKF algorithm. The UKF uses $(2n + 1)$ critical points for n number of states in the filter to transform the mean and covariance without the need to linearize the system. These critical points, often referred to as sigma points for their natural distribution about the mean state estimate, have certain weighting methods to ensure the preservation of the first two moments of the normal distribution [21]. If weighted properly, the sigma points will affect higher moments of the distribution but keep the mean and covariance of the estimate intact. For this study, a symmetric weighting method is used, and the sigma points are weighted using Equation (3.1):

$$w_m^0 = w_c^0 = \frac{\kappa}{n + \kappa} \tag{3.1a}$$

$$w_m^j = w_c^j = \frac{1}{2\left(n + \kappa\right)} \quad \text{for} \quad j = 1, ..., 2n \tag{3.1b}$$

where κ is a scalar weighting variable and n is the number of states in the system. As discussed in [7] and [21], the UKF can match up to fourth order terms in the distribution if the equation $\kappa + n = 3$ is satisfied, and the UT will not work for complex sigma points, so $\kappa > \text{-}n$ is the lower bound for setting the weighting

variable. Therefore, for all of the orbit estimation scenarios run in this study, we will set $\kappa = 3$ - n for n states.

An extensive step by step algorithm for both the EKF and UKF used in this study can be found in Appendix A, and many other research in this topic derive similar algorithms: the EKF in [7] and [11], and the UKF in [7] and [51].

3.2.2 VSD Algorithm

The adaptability of the VSD filter is pivotal in the maneuver detection process. As stated in Section 2.2.2, the VSD filter accounts for major changes in the dynamical system by adding or removing states from the equations of motion. Within the scope of this study, the only states being added in the VSD filter are the two components of the thrust vector during the maneuver of the target, assuming in-plane motion. The algorithm also makes the assumption that the thrust vector is constant throughout each maneuver detection scenario. This causes some inherent error in the thrust estimate because the acceleration of the target due to a constant thrust changes slightly over time based on the mass lost by burning propellant. For the purposes of this study, the thrust states are assumed constant, and for most scenarios the target is assumed to produce a constant acceleration due to thrust. Although the fact that the target is maneuvering is tracked by the VSD filter, more specific parameters such as an estimate for the thrust magnitude and the process noise of the new dynamics is more accurately estimated through a multiple model framework.

3.2.3 IMM Algorithm

The IMM algorithm is used in this study to effectively estimate the process noise of the new dynamics applied during a detected maneuver. A more accurate

assessment of this process noise allows for a more accurate representation of the thrust magnitude and the amount of time spent maneuvering. As discussed in Section 2.2.1, the IMM framework allows a band of VSD filters with different noise assumptions to estimate the future state of the system simultaneously. The interacting component of the algorithm compares the estimates from every VSD in a PDF, finding a combination of the most likely estimate based on the minimization of the MD shown in Equation (2.11). A multivariate normal PDF is used in this study to calculate the model likelihood, and the probability update function is shown in Equation (3.2) [30]:

$$\Lambda_i^k = \mathcal{N}\left(\nu_i^k; 0, \mathbf{S}_i^k\right) = \frac{1}{\sqrt{|2\pi \mathbf{S}_i^k|}} e^{\frac{-1}{2}\left(\nu_i^k\right)^T \left(\mathbf{S}_i^k\right)^{-1} \nu_i^k} \tag{3.2a}$$

$$\mu_i^k = \frac{\mu_{i-1}^k \Lambda_i^k}{\displaystyle\sum_{j=1}^{N} \mu_{i-1}^j \Lambda_i^j}. \tag{3.2b}$$

Here Λ_i^k is the model likelihood and μ_i^k is the model weight for each model k at time t_i. After each model weight is calculated, the weighted state, covariance, and MD at time t_i are calculated using Equation (3.3) [30].

$$\underline{\mathbf{x}}_i = \sum_{k=1}^{N} \mu_i^k \hat{\mathbf{x}}_i^k \qquad \underline{\Psi}_i = \sum_{k=1}^{N} \mu_i^k \Psi_i^k \tag{3.3a}$$

$$\underline{\mathbf{P}}_i = \sum_{k=1}^{N} \mu_i^k \left[\hat{\mathbf{P}}_i^k + \left(\hat{\mathbf{x}}_i^k - \underline{\mathbf{x}}_i\right)\left(\hat{\mathbf{x}}_i^k - \underline{\mathbf{x}}_i\right)^T\right] \tag{3.3b}$$

where $\hat{\mathbf{x}}_i^k$ and $\hat{\mathbf{P}}_i^k$ are the updated state and covariance for each model k at time t_i. This study will look at two different methods for updating the model weights for the IMM algorithm. For the full interacting method using the VSD in real-time, the

39

mixing probabilities will be calculated and a single weighted state and covariance will be fed into each model at every time step, as seen in Equations (3.2) and (3.3) and in Figure 4.
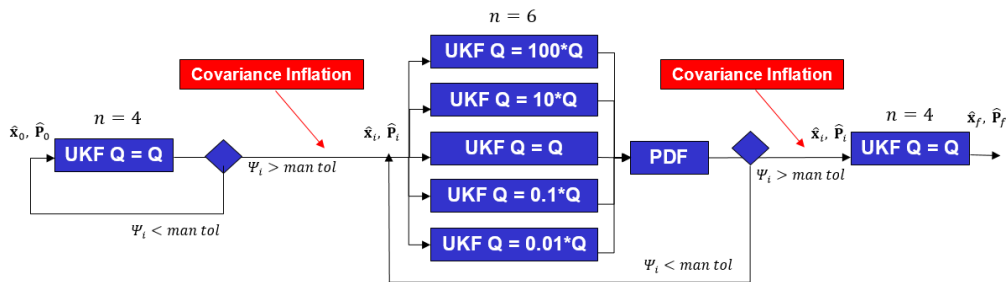
Figure 4. Visual diagram of the VSD IMM algorithm

As discussed in Section 2.2.1, covariance inflation is a key requirement for algorithm convergence whenever the VSD filter is activated pre-maneuver or deactivated post-maneuver [11]. The VSD IMM algorithm is shown to be more accurate than a single filter [7], but is highly sensitive to small changes in the residual vector and the measurement covariance, which can be problematic for large maneuvers.

Another classical MMAE technique that will be explored in this study involved post-processing the model weights after each model filters through the scenario individually. The model weights and update equations do not change, but the models run separate from each other, only calculating the weighted state and covariance a posteriori. This can prevent certain model sensitivities compared to a full interactive method, but cannot be paired with a VSD and applied to real-time maneuver detection [30]. Instead, this classical IMM algorithm will estimate the thrust vector throughout the entire scenario. Although there will be some inherent error as the models are estimating a thrust even when the target is not thrusting, if the thrust magnitude is large enough we will be able to delineate between the thrust

vector outputted by the target and the ambient noise of the estimator. The full step by step IMM algorithm used in this study can be found in Appendix A.

For the purposes of this research and relating to the IMM algorithm analysis in [30], the classical post-processing IMM algorithm is referred to as the first generation (1G) IMM algorithm, while the full VSD IMM algorithm is referred to as the second generation second generation (2G) IMM algorithm. A visual representation of the 1G IMM algorithm can be seen in Figure 5.
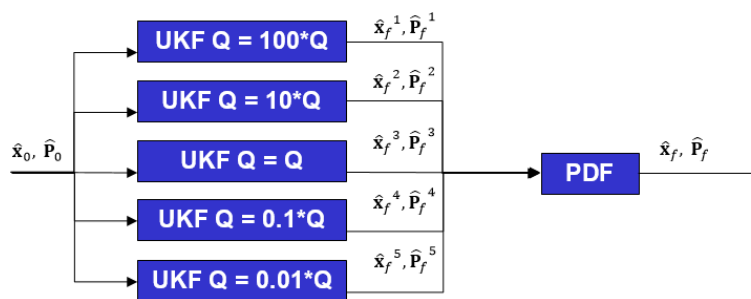
Figure 5. Visual diagram of the 1G IMM algorithm

As shown in both Figure 4 and Figure 5, the IMM framework utilizes five models with process noise covariance hypotheses varying at orders of magnitude from the adjacent models in the framework. The number of models and the distribution of hypotheses is taken from previous research [7], and for each specific scenario the central process noise covariance is adjusted to ensure improved interaction of the models and overall convergence of each algorithm. Although this framework allows for a wider range of estimates regarding the confidence in the dynamics of the system, there is still the risk of the algorithm diverging if the actual process noise is outside the range of noise estimates made in the filter models. Analysis regarding the number of models and the distribution of the hypotheses for each model in the IMM algorithm is beyond the scope of this study. More analysis

regarding algorithm convergence based on the assumptions of each scenario is discussed in Chapter 4.

3.3 Scenario Simulation

The following sections discuss how each of the RPO scenarios examined in this study will be initialized, validated, and analyzed within the scope of this study. The scenarios assessed for this research are run using a coding framework written in MATLAB. For the sake of continuity between the algorithm, code, and post analysis, unless otherwise stated, all measurements and estimates are presented in meters, meters per second, or meters per second per second when describing relative position, velocity, and acceleration, respectively.

3.3.1 Initial Conditions and Noise Factors

Each scenario initializes in the LVLH frame centered on an observer in a circular GEO orbit with a semi-major axis of $a = 4.2164 \times 10^7$ m. This orbit has a period of T = 86164 sec (24 hrs), and a constant mean motion of n = 7.2921×10^{-5} rad/sec. For most scenarios, the target spacecraft starts in an NMC around the chief and is assumed to exhibit no out of plane motion. The initial state vector used for the estimation algorithm is shown in Equation (3.4a), and the state vector for the VSD is shown in Equation (3.4b):

$$\mathbf{x} = [x_0, y_0, \dot{x}_0, \dot{y}_0]^T \tag{3.4a}$$

$$\mathbf{x} = [x, y, \dot{x}, \dot{y}, T_x, T_y]^T . \tag{3.4b}$$

Here x and y represent the radial and along-track position of the target with respect to the observer, and T_x and T_y refer to the relative thrust acceleration vector of the target. The state vector is initialized using the conditions shown in Equation (3.5) represent an NMC starting in the radial direction:

$$x_0 = x_0 \qquad y_0 = 0$$
$$\dot{x}_0 = 0 \qquad \dot{y}_0 = -2nx_0. \tag{3.5}$$

where the initial position in the radial direction, x_0, is defined in this study as the relative trajectory parameter. To ensure convergence of the estimator for each scenario, a large covariance matrix is initialized. The initial state estimation error is assumed to be 10% of the nominal values, with the initial covariance matrix shown in Equation (3.6) [13]:

$$\mathbf{P}_0 = \begin{bmatrix} \sigma_{xx}^2 & 0 & 0 & 0 \\ 0 & \sigma_{yy}^2 & 0 & 0 \\ 0 & 0 & \sigma_{\dot{x}\dot{x}}^2 & 0 \\ 0 & 0 & 0 & \sigma_{\dot{y}\dot{y}}^2 \end{bmatrix} = \begin{bmatrix} \left(\frac{0.1}{n}\right)^2 m^2 & 0 & 0 & 0 \\ 0 & \left(\frac{0.1}{n}\right)^2 m^2 & 0 & 0 \\ 0 & 0 & 0.1^2 \frac{m^2}{sec^2} & 0 \\ 0 & 0 & 0 & 0.1^2 \frac{m^2}{sec^2} \end{bmatrix}. \tag{3.6}$$

Each σ is the standard deviation of each respective state, and n is the mean motion of the chief spacecraft. Because the covariance matrix is constantly updated through each time step as seen in Equation (2.8b), the initial covariance is not as significant as other parameters when analyzing the sensitivity of the estimation algorithm. This initial covariance is used in all of the scenarios demonstrated in this study unless otherwise stated that covariance inflation is necessary for convergence.

The last two parameters needed to initialize the estimator are the process noise and the measurement noise. The measurement noise covariance is initialized based

on the types of measurements used in each scenario. Equation (3.7) shows the different measurement basis functions that will be tested in this study as well as their corresponding measurement noise covariances.

$$
\mathbf{y} = \begin{bmatrix} \rho \\ \alpha \end{bmatrix} = \begin{bmatrix} \sqrt{x^2 + y^2} \\ \arctan \frac{y}{x} \end{bmatrix} \qquad \mathbf{R}_i = \begin{bmatrix} \rho * \sigma_\rho^2 & 0 \\ 0 & \sigma_\alpha^2 \end{bmatrix} \tag{3.7a}
$$

$$
\mathbf{y} = \begin{bmatrix} \rho \\ \dot{\rho} \end{bmatrix} = \begin{bmatrix} \sqrt{x^2 + y^2} \\ \frac{x\dot{x}+y\dot{y}}{\sqrt{x^2+y^2}} \end{bmatrix} \qquad \mathbf{R}_i = \begin{bmatrix} \rho * \sigma_\rho^2 & 0 \\ 0 & \rho * \sigma_{\dot{\rho}}^2 \end{bmatrix} \tag{3.7b}
$$

$$
\mathbf{y} = \begin{bmatrix} \rho \\ \dot{\rho} \\ \alpha \end{bmatrix} = \begin{bmatrix} \sqrt{x^2 + y^2} \\ \frac{x\dot{x}+y\dot{y}}{\sqrt{x^2+y^2}} \\ \arctan \frac{y}{x} \end{bmatrix} \qquad \mathbf{R}_i = \begin{bmatrix} \rho * \sigma_\rho^2 & 0 & 0 \\ 0 & \rho * \sigma_{\dot{\rho}}^2 & 0 \\ 0 & 0 & \sigma_\alpha^2 \end{bmatrix} \tag{3.7c}
$$

Each σ corresponds to the standard deviation of the respective measurement. Each range and range rate covariance is scaled by the range measurement itself, relating to the assumption that the accuracy of a range sensor is inversely proportional to the relative distance from the observer to the target [13].

For this study, the process noise covariance is initialized using a single variable, which simplifies the tuning of this highly sensitive noise factor. The initial process noise covariance is shown in Equation (3.8):

$$
\mathbf{Q} = q_0 \mathbf{I}_{4X4}. \tag{3.8}
$$

Here q_0 is a scaling factor that is analyzed and tuned for nearly every scenario to ensure the convergence of the error residual. For the purposes of this study, the $\mathbf{Q}$ matrix is assumed to be constant once initialized, but the IMM algorithm will

attempt to characterize changes in the process noise by making multiple hypotheses for the **Q** matrix in each model of the IMM algorithm.

3.3.2   Parameter Study for Maneuver Detection

The IMM algorithm is tested and analyzed using a variety of parameters than constitute different types of orbits and maneuvers that a target could exhibit with respect to the observer. The parameters that are analyzed in this study are relative trajectory, maneuver thrust magnitudes, data rate, data type, and measurement noise. For each of these parameters, three nominal values are presented with the hypotheses of good, medium, and poor algorithm performance.

As shown in Equation (3.5), the relative trajectory of the target is expressed in the initial radial position for each scenario. The nominal values for this parameter used in this study are shown in Equation (3.9):

$$x_0 = \begin{bmatrix} 100\,m \\ 1000\,m \\ 10000\,m \end{bmatrix}.$$

(3.9)

For the maneuver magnitude parameter, there is no hypothesis relating to the performance of the IMM algorithm, but rather a small, medium, and large maneuver. Although this parameter relates to the magnitude of the thrust, the thrust vector itself may change for each scenario, which should not affect performance. The maneuver magnitude nominal values are shown in Equation (3.10):

$$T = \sqrt{T_x^2 + T_y^2} = \begin{bmatrix} 0.001\frac{m}{sec^2} \\ 0.01\frac{m}{sec^2} \\ 0.1\frac{m}{sec^2} \end{bmatrix}.$$

(3.10)

The data rate parameter constitutes the frequency at which measurements are collected and read into the estimator. Although Section 2.4.2 discussed instances of large data gaps in an RPO scenario, for the purposes of this study the data rate is assumed to be constant. The data rate nominal values are shown in Equation (3.11), here represented as a time gap between each measurement:

$$\delta t = t_i - t_{i-1} = \begin{bmatrix} 1 \ sec \\ 10 \ sec \\ 120 \ sec \end{bmatrix}. \tag{3.11}$$

The data types that form the measurement basis function for each scenario are shown in Equation (3.7), but the measurement noise covariances are defined by Equation (3.12) in terms of a good, average, and poor sensor. The good sensor is related to notional values in [13] meant to represent 1 cm of error and 0.1 cm of error in the range and range rate measurements, respectively. Each worsening sensor is simply given an order of magnitude of increasing error.

$$\sigma_{good} = \begin{bmatrix} 1 \times 10^{-5} \ m \\ 1 \times 10^{-6} \ \frac{m}{sec} \\ 0.05^o \end{bmatrix} \quad \sigma_{average} = \begin{bmatrix} 1 \times 10^{-4} \ m \\ 1 \times 10^{-5} \ \frac{m}{sec} \\ 0.10^o \end{bmatrix} \quad \sigma_{poor} = \begin{bmatrix} 1 \times 10^{-3} \ m \\ 1 \times 10^{-4} \ \frac{m}{sec} \\ 0.25^o \end{bmatrix} \tag{3.12}$$

Within the scope of this research, these notional error values do not relate in any way to any operational space-based sensor performances. Each sensor is given a nominal deviation for range, range rate, and azimuth measurements, but each scenario will use the proper deviation values depending on what data types are available.

3.3.3   Kalman Filter Validation

Before delving into the complex IMM algorithms used in this study, the EKF and UKF are validated to ensure a baseline relative satellite motion scenario for error comparison. Desai shows that the EKF has acceptable levels of error for relative satellite orbit determination [13]. Desai uses two primary metrics to assess performance that are also used extensively in the current study: root mean squared error (RMSE), and time-based plots. RMSE calculates an average error over the course of the entire scenario, which can indicate the overall performance for each scenario. Time plots are necessary to analyze trends in the state errors over time that the RMSE cannot capture. Time plots also track estimated thrust values and model weights for each model in each IMM algorithm. Table 3 shows the initial parameters used for the baseline validation scenario.

Table 3. Initial parameters for baseline scenario

Parameter	Value
Scenario length (sec)	2000
Initial relative trajectory (m)	1000
Data rate (sec^{-1})	1
Data type	$[\rho \; \dot{\rho} \; \alpha]$
Sensor Quality	good
Q_0	1×10^{-9}

This baseline scenario as well as every scenario presented in the current study uses a ×100 Monte Carlo simulation to ensure random noise factors are suppressed and data trends can be accurately analyzed. As shown in Table 4, Both the UKF and EKF implemented in the current study have comparable levels of average error with respect to the literature using similar initial conditions [13].

Table 4. Simulation results for baseline scenario

RMSE	UKF	EKF	Desai
δx (m)	0.012	0.047	0.112
δy (m)	0.094	0.27	0.109
$\delta\dot{\text{x}}$ (m/s)	$5.2{\times}10^{-5}$	$1.9{\times}10^{-3}$	$1.01{\times}10^{-3}$
$\delta\dot{\text{y}}$ (m/s)	$2.9{\times}10^{-3}$	0.013	$6.33{\times}10^{-4}$

The RMSE values shown in Table 4 are utilized throughout Chapter 4 to assess the performance of adaptive estimation techniques with non-cooperative maneuvers.

3.4   Summary

This chapter covers the methodology used to answer the three research questions listed in Chapter 1. Outlined in this chapter are the specific parameters developed from the success criteria for each research question as well as a descriptive discussion into the procedures and algorithms used for this study. The results of each maneuver detection scenario as well as an in-depth analysis and discussion regarding algorithm performance is detailed in the Chapter 4.

IV. Results and Analysis

The following chapter investigates the adaptive estimation techniques outlined in Section 3.2 and their applications to maneuver detection and characterization of a target spacecraft operating in close proximity to an observer spacecraft. The performance of both a 1G and 2G IMM algorithm is assessed through a variety of scenario parameters outlined in Section 3.3.2. The results of each scenario are evaluated based on the research questions defined in Section 1.2.

Throughout the different sections of this chapter, different algorithms are implemented and different setups are used based on the iterative analysis of the current research. Table 5 summarizes the specific algorithms used on the scenarios displayed in each section of this chapter, including what type of filters are studied and whether the thrust acceleration vector is being estimated or not.

Table 5. The algorithms and filters used for each results section

Section	IMM type	EKF?	UKF?	Thrust states
4.1	2G	no	yes	VSD
4.2	1G	yes	yes	off
4.3	1G	yes	yes	on
4.4	1G	no	yes	on

For the purposes of this research, all parameters and scenarios displayed in this chapter are notional values derived from previous works [7, 13] without any indication or analysis relating to the mission of either spacecraft. Despite the goals and motivations of this research, no operational data is applied to this study.

4.1 Maneuver Detection Analysis

This section applies a 2G IMM algorithm using VSD filters with varying levels of process noise to detect and characterize a continuous maneuver in relative spacecraft motion. Because of the highly nonlinear aspects of the VSD IMM framework, the EKF was unable to converge for these scenarios. Therefore, the UKF is the only filter presented with the VSD IMM algorithm.

The first scenario shows a comparison between a single VSD filter and a bank of VSD filters in an IMM framework. Both scenarios run a single UKF before the detected maneuver start time and after the detected maneuver stop time. The VSD filter estimates the thrust acceleration in both the radial and along-track directions with respect to the observer. The parameters for the first scenario are shown in Table 6.

Table 6. Initial parameters for maneuver detection scenario 1

Parameter	Value
Thrust acceleration (mm/s^2)	100
Thrust duration (s)	100
Scenario length (s)	1500
Initial relative trajectory (m)	1000
Data rate (sec^{-1})	1
Data type	$[\rho \; \alpha]$
Sensor Quality	good
Q_0	1×10^{-10}

Table 7 shows the RMSE values in the first maneuver detection scenario for a single VSD filter compared to a bank of VSD filters in an IMM framework. Both techniques have zero or minimal error in detecting the maneuver start time and

estimating maneuver duration, which can be attributed to a high immediate change in the dynamics caused by a large target maneuver. Both techniques also converge on an accurate thrust acceleration vector for the 100 seconds that the VSD filters are active.

Table 7. Simulation results for maneuver detection scenario 1

RMSE	Single UKF	IMM UKF
δx (m)	1.23×10^3	0.35
δy (m)	4.26×10^3	0.19
$\delta\dot{x}$ (m/s)	1.97	0.011
$\delta\dot{y}$ (m/s)	6.54	0.049
δT (m/s^2)	6.01×10^{-4}	5.03×10^{-4}
Man start (s)	0	0
Man duration (s)	1.78	0

The IMM VSD algorithm holds RMSE values comparable to the baseline scenario, while the single VSD filter has RMSE position values on the order of kilometers. Figure 6a shows that the position errors using a single VSD filter increase through the maneuver and continue to increase post maneuver, while Figure 6b shows that the position errors using the VSD filter with an IMM framework stabilize or decrease post-maneuver.
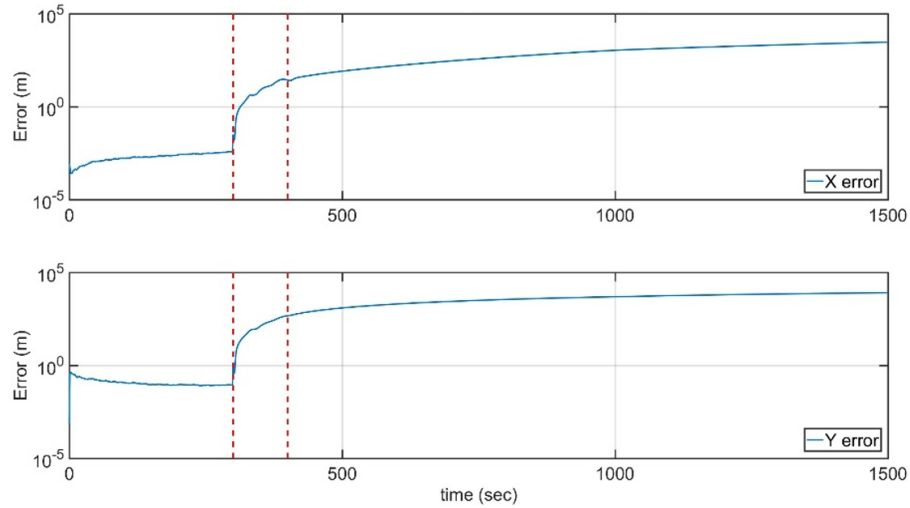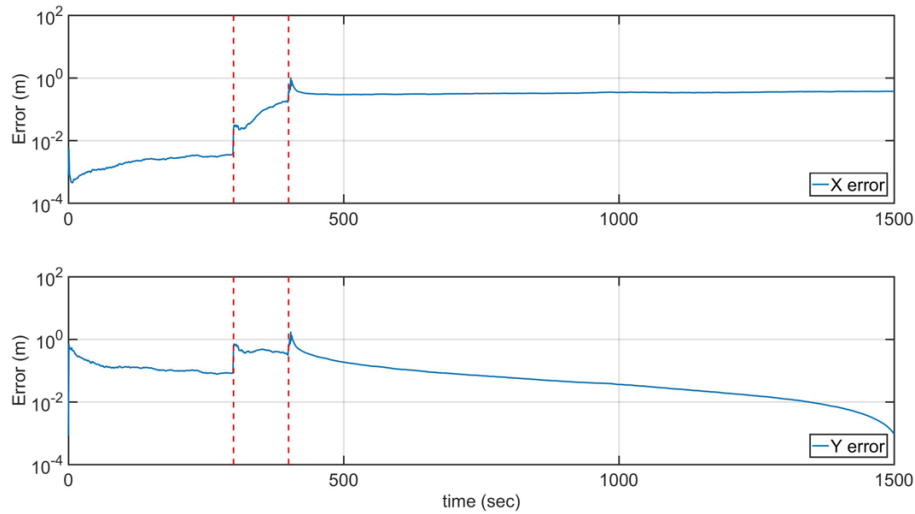
Figure 6. Position errors for maneuver detection scenario 1 with (a) a single VSD filter and (b) IMM VSD filters; dashed lines indicate the target maneuver

Multiple iterations and attempts at understanding the 2G IMM algorithm show that maneuver detection using adaptive estimation is highly sensitive to changing scenario parameters. For this scenario, the VSD IMM algorithm fails to converge with a data rate less than one measurement per second and a data type different than range and azimuth, and worsening sensors seem to be correlated with higher

52

estimated state errors. The 2G algorithm typically diverges when the covariance matrix of each model becomes too small, breaking the positive definite requirement for the PDF. Large data gaps equates to a longer propagation of the dynamics, and with the thrust vector added to the dynamics more unanticipated error could explain the diverging filters. More scenarios exploring these changing parameters can be found in Appendix B.

Along with RMSE values and state error trends, some changing parameters affect how quickly the VSD IMM algorithm detects a maneuver start and stop time. A decrease in the target maneuver magnitude appears to be correlated with an increase in the maneuver detection time error, leading to a maneuver magnitude lower limit for the VSD IMM algorithm to detect a maneuver. Table 8 shows the initial parameters for a scenario where the VSD IMM algorithm is unable to effectively detect and track a maneuver.

Table 8. Initial parameters for maneuver detection scenario 2

Parameter	Value
Thrust acceleration (mm/s^2)	1
Thrust duration (s)	400
Scenario length (s)	2000
Initial relative trajectory (m)	1000
Data rate (sec^{-1})	1
Data type	$[\rho \; \alpha]$
Sensor Quality	good
Q$_0$	1×10^{-12}

As shown in Table 9, the RMSE values for each state remain relatively low in this scenario, and the VSD IMM algorithm is able to detect the maneuver start within seconds of error.

Table 9. Simulation results for maneuver detection scenario 2

RMSE	IMM UKF
δx (m)	0.086
δy (m)	0.24
$\delta\dot{\text{x}}$ (m/s)	2.9×10^{-3}
$\delta\dot{\text{y}}$ (m/s)	0.039
δT (m/s^2)	8.22×10^{-4}
Man start (s)	6.36
Man duration (s)	1.29×10^{3}

However, the VSD IMM algorithm never detected a maneuver stop time, estimating a maneuver magnitude long after the target stopped maneuvering. As shown in Figure 7a, the maneuver detection statistic spikes around both the maneuver start time and the maneuver stop time but never reaches the maneuver detection threshold that signals the VSD to stop estimating a thrust vector. However, continuously estimating the thrust vector post-maneuver does not seem to affect the RMSE values of the scenario. Time plots show roughly a 10% increase in error post maneuver but an overall recovery of the state error to baseline levels. As shown in Figure 7b, the VSD filters continue to estimate a thrust vector post-maneuver, capturing the small maneuver magnitude and reaching a zero steady state thrust through the end of the scenario.
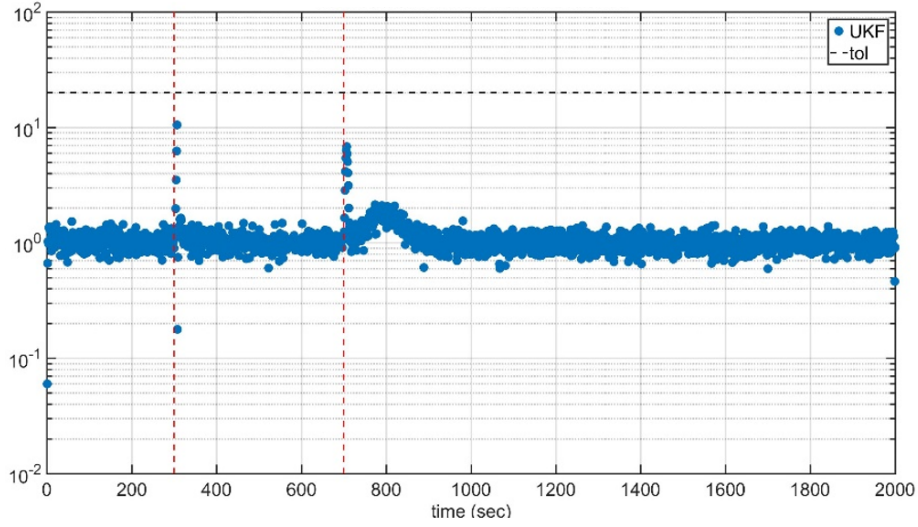
(a)
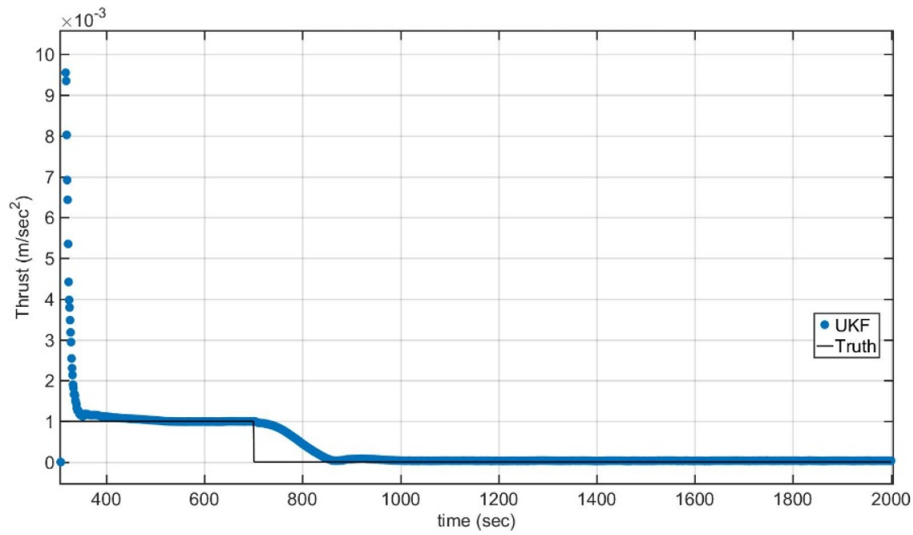
(b)

Figure 7. For maneuver detection scenario 2 (a) the maneuver detection statistic and (b) the thrust magnitude estimate vs truth

The second maneuver detection scenario opens a new level of investigation for testing the performance of an IMM algorithm based on the claim that small target maneuvers may not need to be detected in order to maintain baseline level state errors.

4.2   Small Maneuver Analysis

The results from applying a 2G IMM algorithm to maneuver detection scenarios show a possibility to handle small target maneuvers using an IMM framework without the need for maneuver characterization. The following section analyzes a small maneuver scenario using a 1G IMM algorithm without adding a thrust acceleration vector to the system dynamics. The 1G IMM algorithm requires a level of post processing that delays real-time analysis, but with the sensitivity of the VSD filter and the PDF, a 1G IMM algorithm may be a more stable alternative given varied scenario parameters. Table 10 shows the initial parameters for the first small maneuver scenario using a 1G IMM algorithm.

Table 10. Initial parameters for small maneuver scenario 1

Parameter	Value
Thrust acceleration (mm/s^2)	1
Thrust duration (s)	400
Scenario length (s)	2000
Initial relative trajectory (m)	1000
Data rate (sec^{-1})	1
Data type	$[\rho \ \alpha]$
Sensor Quality	good
Q$_0$	1×10^{-8}

Along with the UKF, the EKF is applied as a viable filter for these scenarios because of the added stability of a constant dynamical model in the 1G IMM algorithm. For the first scenario, an RMSE comparison does not show the difference between a single filter and a series of IMM filters because the small maneuver does not drastically change the dynamics from the baseline scenario. However, the

maneuver detection statistic shows a clear difference between the single filter and IMM filters, as shown in Figure 8a and 8b.
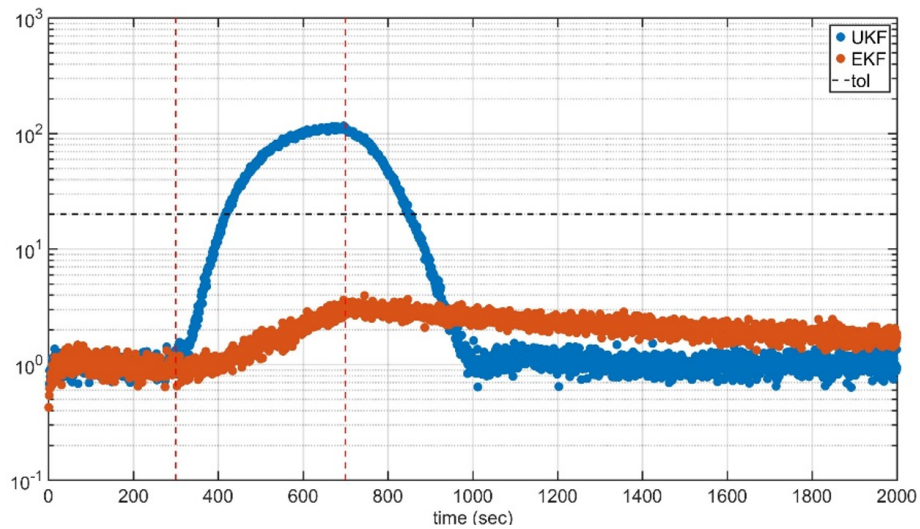
(a)
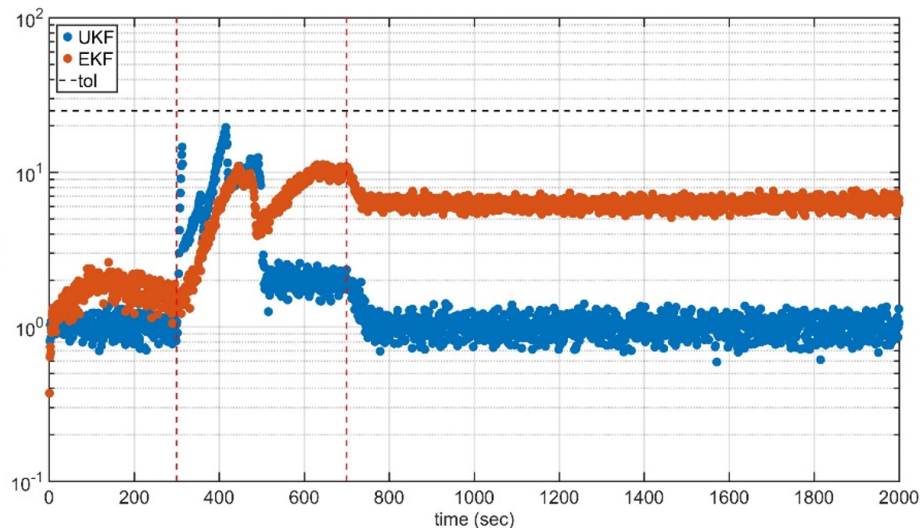
(b)

Figure 8. Maneuver detection statistic for small maneuver scenario 1 with (a) a single filter and (b) IMM filters; dashed lines indicate the target maneuver

Using the 1G IMM framework, the maneuver detection statistic remains below the maneuver threshold throughout the entire scenario, while the single UKF filter arcs over the maneuver threshold for a significant amount of scenario time. Recall

from Equation (2.11) that the MD is used as the maneuver detection statistic in this research:

$$\Psi_k = \bar{\mathbf{r}}^T \mathbf{S}_k^{-1} \bar{\mathbf{r}}. \tag{4.1}$$

The large increases in the MD of each filter shown in Figure 8 could either mean the residuals are increasing or the residual covariance matrix is decreasing. Despite the instability during the maneuver in Figure 8b, both a series of UKF and EKF filters in a 1G IMM framework hold reasonable state errors without ever detecting a maneuver.

The primary benefit of a 1G IMM algorithm compared to the 2G IMM algorithm is an increased ability to handle changes in different scenario parameters due to the level of post-processing present in the 1G IMM algorithm. The next maneuver scenario analyzes a few changes in these parameters compared to the previous scenarios, shown in Table 11.

Table 11. Initial parameters for small maneuver scenario 2

Parameter	Value
Thrust acceleration (mm/s^2)	1
Thrust duration (s)	400
Scenario length (s)	2000
Initial relative trajectory (m)	1000
Data rate (sec^{-1})	10
Data type	$[\rho\ \alpha]$
Sensor Quality	poor
Q_0	1×10^{-5}

The second small maneuver scenario takes into account a slower data rate as well as a poor sensor quality, causing a higher initial process noise covariance for sufficient results. These worsening parameters appear to correlated with higher RMSE values compared to the baseline scenario, as shown in Table 12. Since the maneuver magnitude and duration is the same between the first and second small maneuver scenarios, the worsening state errors do not appear to be correlated with the small target maneuver.

Table 12. Simulation results for small maneuver scenario 2

RMSE	Single UKF	Single EKF	IMM UKF	IMM EKF
δx (m)	0.89	1.56	0.76	1.34
δy (m)	5.40	3.27	2.41	3.39
$\delta\dot{\text{x}}$ (m/s)	4.1×10^{-3}	7.1×10^{-3}	6.5×10^{-3}	9.3×10^{-3}
$\delta\dot{\text{y}}$ (m/s)	0.071	0.23	0.046	0.24

The small maneuver scenarios serve as a validation of an alternative adaptive estimation technique that does not involve the sensitive process of maneuver detection. In scenarios where small target maneuvers are expected, adding an adaptive estimation framework to relative orbit estimation allows an observer to continue to track a maneuvering target without attempting to detect or characterize the maneuver. However, the current study claims that maneuvers are well characterized with improved state errors using adaptive estimation with the thrust acceleration vector added as states to the system.

4.3 Maneuver Characterization Analysis

The 1G IMM algorithm is primarily utilized in this study as a means of maneuver characterization. Compared to maneuver detection, maneuver

characterization focuses on capturing the target thrust acceleration vector and analyzing the target maneuver in terms of magnitude and duration.

The first maneuver characterization scenario uses the exact same initial scenario parameters as the first small maneuver scenario, shown in Table 10, but the filters for this scenario are now permanently estimating a target maneuver as acceleration states in both the radial and along-track directions. As shown in Table 13, both the UKF and EKF filters in a 1G IMM framework have improved RMSE values compared to the single UKF and EKF filters. The results using the 1G IMM algorithm show that even in instances of small target maneuvers, estimating a thrust acceleration for the entire scenario can accurately characterize a small maneuver while maintaining lower state errors compared to not estimating a maneuver at all.

Table 13. Simulation results for maneuver characterization scenario 1

RMSE	Single UKF	Single EKF	IMM UKF	IMM EKF
δx (m)	0.89	1.56	0.11	0.41
δy (m)	5.40	3.27	0.24	0.84
$\delta\dot{\text{x}}$ (m/s)	4.1×10^{-3}	7.1×10^{-3}	4.9×10^{-3}	0.011
$\delta\dot{\text{y}}$ (m/s)	0.071	0.23	0.013	0.15
T_x (m/s^2)	0.013	$1.6\text{e}\times10^{-5}$	1.1×10^{-4}	1.6×10^{-5}
T_y (m/s^2)	0.030	$3.1\text{e}\times10^{-3}$	4.7×10^{-4}	6.6×10^{-4}

Along with keeping the state RMSE values at baseline levels, the 1G IMM algorithm is highly efficient at characterizing maneuvers compared to single filter estimators. As shown in Figure 9a, the small 1 mm/s^2 maneuver is below the inherent noise of the single UKF filter, and the single EKF filter converges quickly to a steady state maneuver magnitude of zero. When these filters are applied to a 1G IMM framework as shown in Figure 9b, the UKF filters can now capture and

characterize the target maneuver, but the EKF filters have no way of quickly adapting to the change in dynamics. Recall that the thrust acceleration vector is assumed to be constant for both IMM algorithms, which can explain the delay in tracking the maneuver for the UKF filters and the failure to characterize the maneuver with EKF filters.
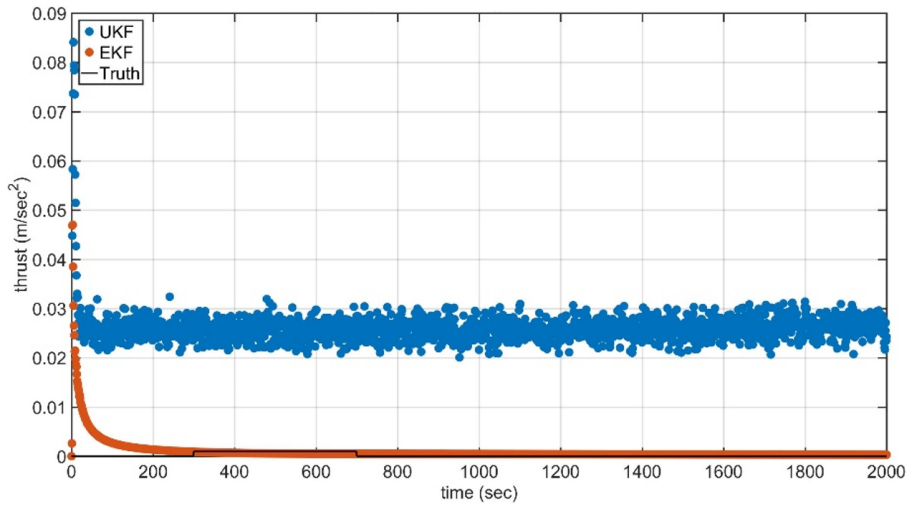
(a)
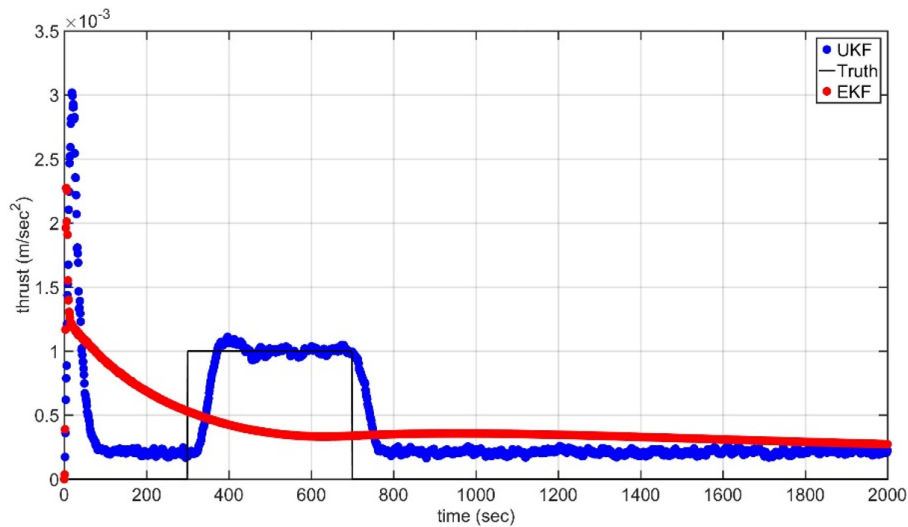
(b)

Figure 9. Thrust acceleration estimate for maneuver characterization scenario 1 with (a) a single filter and (b) IMM filters

The fact that the EKF filter cannot react quickly to a target maneuver causes problems in maneuver characterization scenarios attempting to capture larger maneuvers. The thrust magnitude for the second maneuver characterization scenario is much larger, shown with the rest of the initial scenario parameters in Table 14.

Table 14. Initial parameters for maneuver characterization scenario 2

Parameter	Value
Thrust acceleration (mm/s^2)	100
Thrust duration (s)	400
Scenario length (s)	2000
Initial relative trajectory (m)	1000
Data rate (sec^{-1})	10
Data type	$[\rho \; \dot{\rho} \; \alpha]$
Sensor Quality	good
Q_0	1×10^{-8}

As seen in Table 15, using single UKFs and EKFs cause the state errors to diverge dramatically, and neither filter can capture an accurate target maneuver profile. These results drastically change when UKFs are used in an IMM framework, but the EKFs are slow to adapt and cause the 1G IMM algorithm to diverge due to a non-positive definite covariance matrix.

Despite the improvement of RMSE values from a single filter to a bank of IMM filters, the IMM UKFs still do not reach error levels comparable to the baseline scenario. This could be caused by the fact that the IMM algorithm continuously estimates the thrust acceleration states long after the maneuver has stopped, effectively contributing to the noise added to the estimator.

62

Table 15. Simulation results for maneuver characterization scenario 2

RMSE	Single UKF	Single EKF	IMM UKF	IMM EKF
δx (m)	2.4×10^2	2.6×10^3	13.30	N/A
δy (m)	3.6×10^2	3.4×10^3	1.05	N/A
$\delta\dot{x}$ (m/s)	5.09	45.8	0.28	N/A
$\delta\dot{y}$ (m/s)	4.50	18.9	0.12	N/A
T_x (m/s^2)	0.11	0.10	3.4×10^{-3}	N/A
T_y (m/s^2)	0.10	0.10	0.013	N/A

The third maneuver characterization scenario relies on the fact that the 1G IMM algorithm can handle more varied scenario parameters compared to the VSD filters in the 2G IMM framework. As shown in Table 16, the data rate for this scenario is lowered to once per every two minutes, which may be indicative of large gaps where sensors are unable to collect accurate measurements.

Table 16. Initial parameters for maneuver characterization scenario 3

Parameter	Value
Thrust acceleration (mm/s^2)	30
Thrust duration (s)	400
Scenario length (s)	5000
Initial relative trajectory (m)	1000
Data rate (sec^{-1})	120
Data type	$[\rho\ \dot{\rho}\ \alpha]$
Sensor Quality	good
Q_0	1×10^{-7}

For this scenario, each filter is affected differently by the larger data gaps. Although the single EKF cannot effectively characterize the maneuver, Table 17 shows that the single EKF has improved performance over a single UKF due to the fact that the UKF does not have enough data to converge quickly on the maneuver or down to zero acceleration when the target is not maneuvering. However, as shown in Figure 10b, the 1G IMM framework allows the UKFs to characterize the target maneuver with limited measurement data, while the EKFs in a 1G IMM framework diverge post-maneuver.

Table 17. Simulation results for maneuver characterization scenario 3

RMSE	Single UKF	Single EKF	IMM UKF	IMM EKF
δx (m)	3.7×10^3	41.79	24.35	N/A
δy (m)	3.9×10^2	8.92	6.04	N/A
$\delta\dot{x}$ (m/s)	30.88	0.84	0.46	N/A
$\delta\dot{y}$ (m/s)	42.06	6.69	0.34	N/A
T_x (m/s^2)	1.59	2.9×10^{-4}	4.8×10^{-3}	N/A
T_y (m/s^2)	2.29	0.010	7.9×10^{-3}	N/A

Despite converging on what seems to be the target maneuver, the UKF IMM algorithm is still nowhere near the RMSE values exhibited in the baseline scenarios. Higher RMSE values could be attributed to the lower data rate, but could also still be the fact that the thrust acceleration state estimates add an extra level of noise to the estimator when the target is not maneuvering. Further sensitivity analysis is required with respect to various sized data gaps indicative of a realistic RPO scenario.
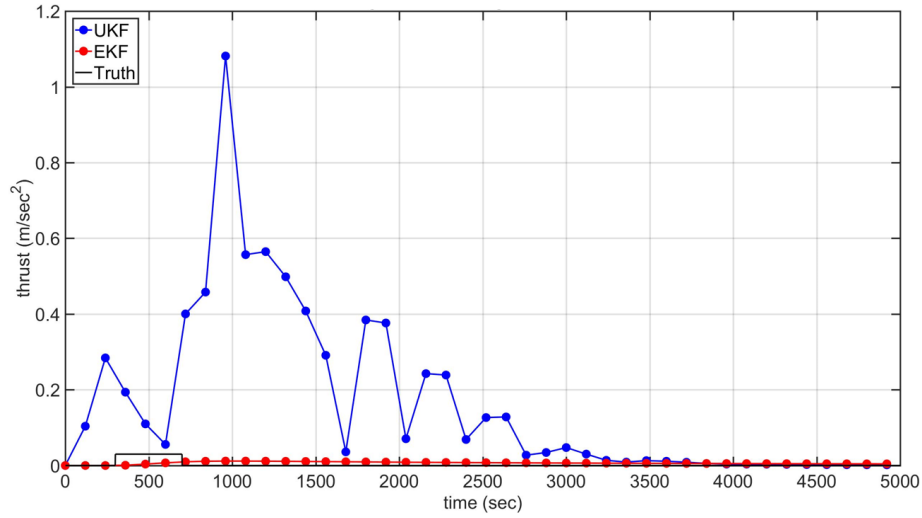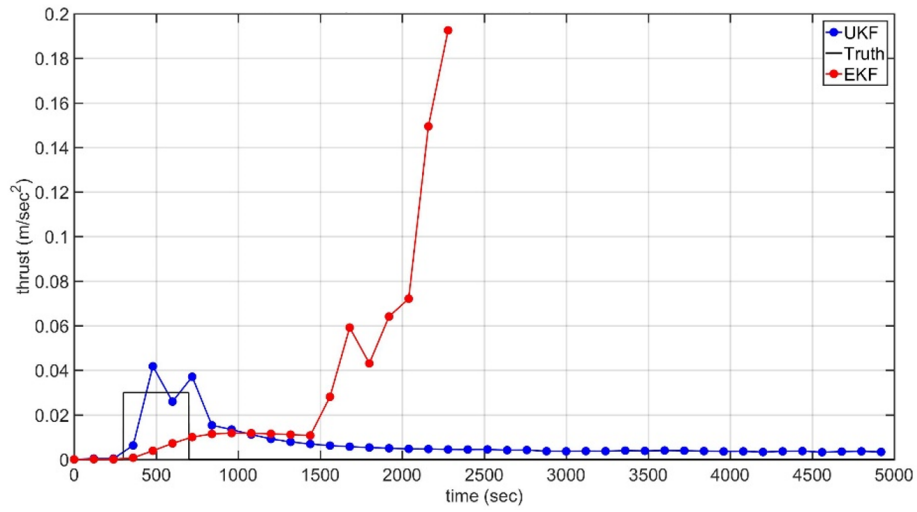
Figure 10. Thrust acceleration estimate for maneuver characterization scenario 3 with (a) a single filter and (b) IMM filters

The maneuver characterization scenarios show the effectiveness of a band of UKFs in a 1G IMM framework and their ability to characterize larger maneuvers with limitations to data rate and sensor type, but the EKFs in an IMM framework do not have enough inherent adaptability to characterize a maneuver effectively.

None of the maneuver characterization scenarios can attain RMSE values comparable to the baseline scenario.

4.4 Dynamic Thrust Analysis

A major assumption used in this research is that the target is exhibiting a constant thrust acceleration for the duration of the maneuver time. Although most spacecraft are designed with propulsions systems that output a constant force, the direction of that force and the subsequent acceleration of the target does not remain constant. However,non-cooperative maneuvers are nearly impossible to accurately predict in terms of both direction and magnitude without information about propulsion capabilities of the target. This section addresses these realistic concerns and attempts to solve them using the 1G IMM algorithm used in the previous section.

The scenario presented in this section is an notional maneuver calculated by the target in an attempt to rendezvous with the observer. The initial scenario parameters are shown in Table 18.

Table 18. Initial parameters for dynamic thrust scenario

Parameter	Value
Thrust acceleration (mm/s^2)	41-43
Thrust duration (s)	3000
Scenario length (s)	3000
Initial relative trajectory (m)	100000
Data rate (sec^{-1})	1-30*
Data type	$[\rho \; \alpha]$
Sensor Quality	good
Q_0	1×10^{-9}

* varying time step based on numerical integration

Because of the inherent limitations to linearizing the system dynamics, the EKF filters in a 1G IMM framework quickly diverge when the system dynamics can only assume a constant thrust vector, so only the UKF filters can be applied to the dynamic thrust scenario. As shown in Table 19, The UKF IMM algorithm has large state RMSE values compared to the baseline scenario.

Table 19. Simulation results for dynamic thrust scenario

RMSE	IMM UKF
δx (m)	37.084
δy (m)	38.30
$\delta\dot{\text{x}}$ (m/s)	0.24
$\delta\dot{\text{y}}$ (m/s)	0.25
T$_x$ (m/s^2)	0.0013
T$_y$ (m/s^2)	0.0010

Despite the target exhibiting a variable thrust vector and the estimator dynamics assuming a constant thrust, the UKF IMM algorithm is able to track the target maneuver throughout the scenario with approximately 1 mm/s^2 worth of error in each direction. Figure 11 shows the thrust acceleration estimates compared to truth data in both the radial and along-track directions.
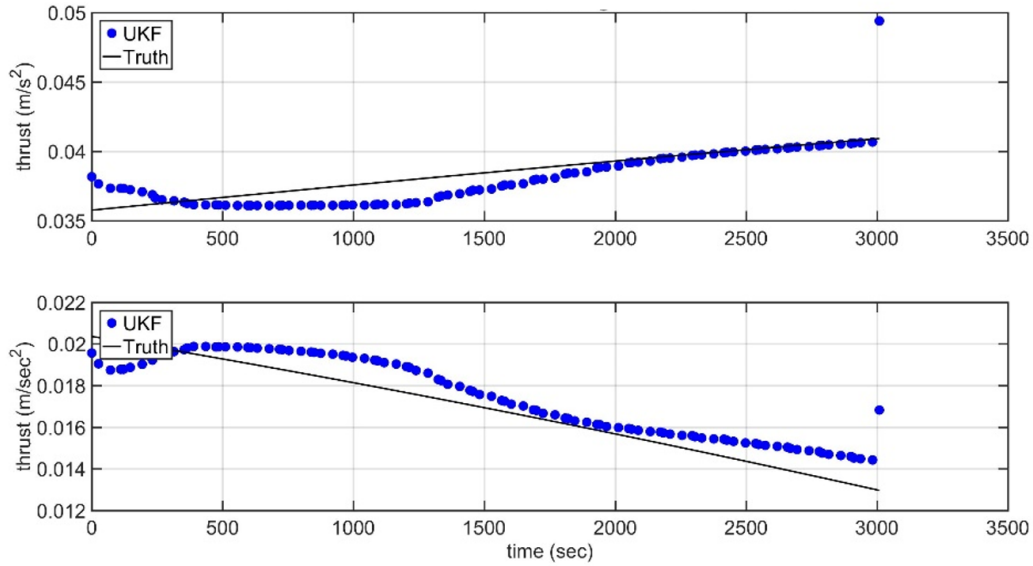
Figure 11. Thrust acceleration estimate for dynamic thrust scenario

The dynamic thrust scenario shows the adaptability of the 1G IMM algorithm and its ability to handle drastic changes in not only the scenario parameters but also the system dynamics. The 1G IMM algorithm is able to capture a relatively accurate thrust acceleration vector for the target at the cost of high state errors relative to the baseline scenario. Improvements to this algorithm can be made if more information is known about the maneuver capabilities of the target spacecraft, which could help estimate the dynamics of the thrust acceleration vector.

4.5 Parameter Study Conclusions

The current study uses five scenario parameters defined in Section 3.3.2 to assess the performance of each adaptive estimation technique used to detect and characterize non-cooperative maneuvers for RPO missions. Overall, the 2G IMM algorithm has higher parameter requirements for convergence in terms of data rate and data type, but both IMM algorithms have varying levels of success in terms of maneuver detection and characterization when experiencing different scenario parameters.

The most prominent parameter analyzed in this study is the target maneuver magnitude. Both IMM algorithms are tested with both large and small relative maneuvers with various results. Overall, the 2G IMM algorithm has more difficulty detecting lower thrust magnitudes but maintains state errors consistent with the baseline scenario. Higher thrust magnitudes appear to be correlated with higher state errors but lower errors in maneuver detection times. The 1G IMM algorithm can effectively characterize maneuvers of various thrust magnitudes, but at the cost of higher state errors than the baseline scenario, especially when other scenario parameters vary.

Decreasing the observer sensor accuracy is most directly correlated with higher state errors for both IMM algorithms, but does not immediately cause convergence issues. As seen in Table 11 and other scenarios with poor sensor accuracy in Appendix B, a worsening sensor accuracy is also correlated with a higher process noise covariance, which conceptually refers to the fact that the estimator has a lower confidence in the system dynamics when it is fed less accurate measurements.

The scenario in Section 4.4 first analyzes changes in relative trajectory of the target. Due to the variable levels of process noise allowed by adaptive estimation, the relative trajectory assumption used in the HCW dynamical equations becomes

invalid before the IMM algorithms fail to converge. Initial analysis of the relative trajectory parameter shows successful scenarios using UKF filters in an IMM framework and nonlinear relative equations of motion. An EKF IMM algorithm using similar dynamics runs into significant issues regarding computation time due to the linearization process necessary in the EKF framework. Further analysis of the IMM algorithms with nonlinear dynamics is shown in Appendix C.

Changes in the data rate parameter can cause significantly higher state errors as well as convergence issues for both IMM algorithms. Any collection rate longer than 1 Hz appears to cause the 2G IMM algorithm to diverge. The 1G IMM algorithm can handle longer gaps between measurements, as seen in Figure 10, but can still experience significantly higher state errors. Conceptually speaking, higher state errors could cause a limit in data type as well if a sensor loses its pointing accuracy on the target.

The data type is the most difficult parameter to change due to significant convergence issues for both IMM algorithms. In this study, the 2G IMM algorithm cannot converge on an accurate maneuver estimate without any other data type besides range and azimuth data. The 1G IMM algorithm can also handle range rate measurements, but as seen in Table 15 there is no significant benefit to the state error by adding this extra measurement. Any limited measurement scenario (range/range rate or angles-only data types) causes a drastic increase in state errors and is not feasible for the applications of adaptive estimation in the current study.

4.6 IMM Algorithm Analysis

The initial analysis of the current study does not focus on the structure of adaptive estimation techniques, but there are observed differences in how the 1G and 2G IMM algorithms calculate the weights for each filter model. As shown in

Figure 12a, only one model dominates the estimation at a time in the 1G IMM algorithm, and significant model switching only takes place while the target is maneuvering. For the 2G IMM algorithm shown in Figure 12b, the model weights are only calculated when the VSD filters are active, and because of the real-time nature of the algorithm there is a significant amount of active interaction between each model.
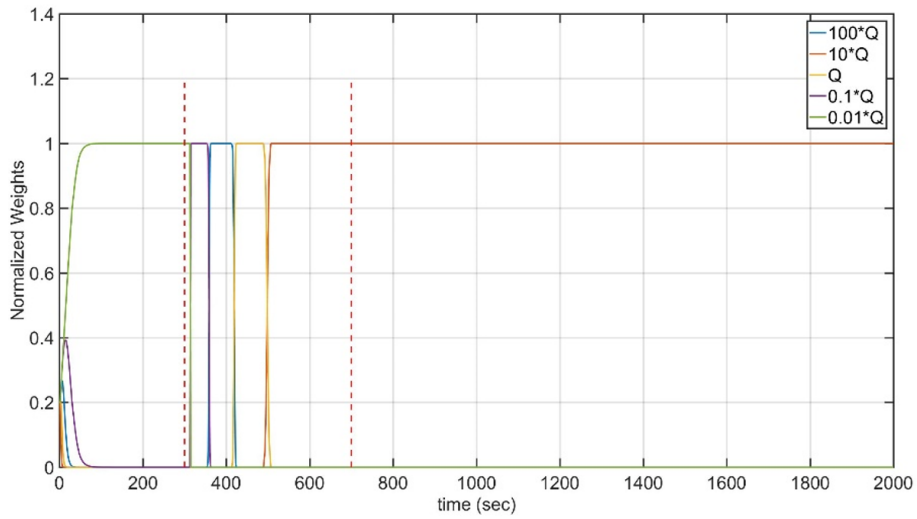

(a)
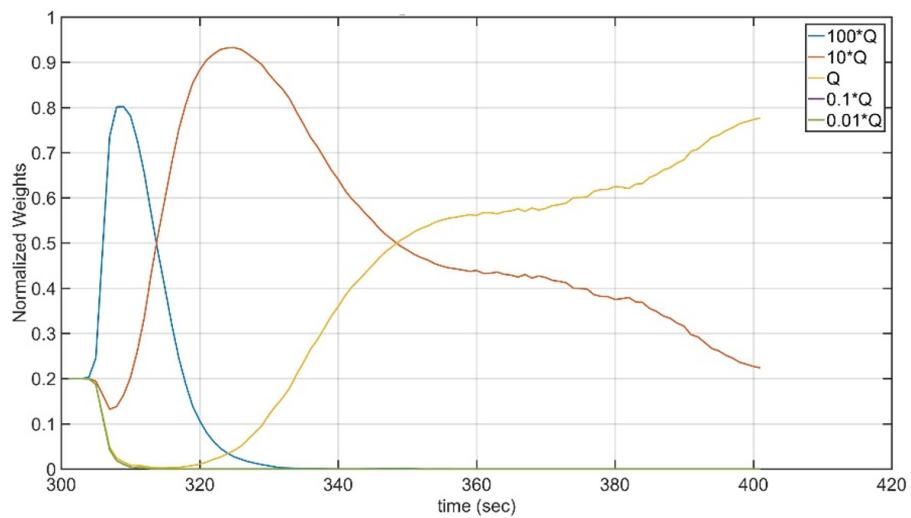
(b)

Figure 12. Typical model weights for (a) a 1G IMM algorithm and (b) a 2G IMM algorithm; dashed lines indicate the target maneuver

Further analysis of the maneuver detection scenarios imply that increased model interaction could be correlated with increasing state errors in the models. Figure 13 shows the model weights for maneuver detection scenarios 3 and 4, results of which can be found in Appendix B. Maneuver detection scenario 3 has low state errors and accurate detection times for the VSD filter, which appears to be correlated with the IMM algorithm converging on a single model, as seen in Figure 13a. Maneuver detection scenario 4 uses poor sensors, which cause higher state errors and a larger error in maneuver detection times. As seen in Figure 13b, the target maneuver stops at 700 seconds, and the small amount of time post-maneuver with the VSD still on sees the most sporadic model interactions. Within the scope of the scenarios analyzed in this study, large deviations between the predicted and the truth dynamical models seem to correlate with more dynamic model interactions to handle the increasing state errors.

Figures 12 and 13 show and initial analysis for the dynamics behind model interactions, but without a clear pattern across all scenarios there is no clear method to predict how the model weights will interact or which model will dominate over the others. Distributing the process noise covariance at an order of magnitude over 5 separate models is taken from [7] without any further analysis due to the similar applications of the adaptive estimation algorithms, but further analysis into the number of models and the distribution of the model hypotheses is beyond the scope of this research. Future work concerning the extended analysis of adaptive estimation is outlined in Section 5.3.
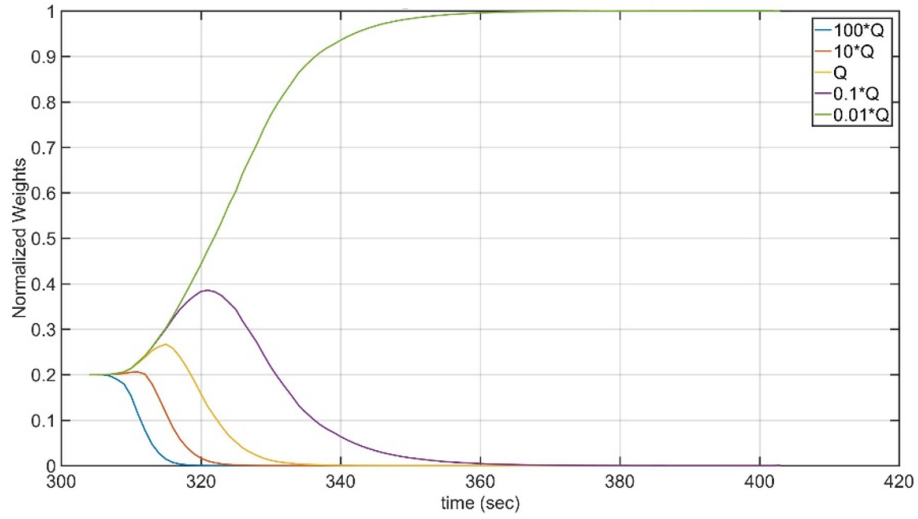
(a)
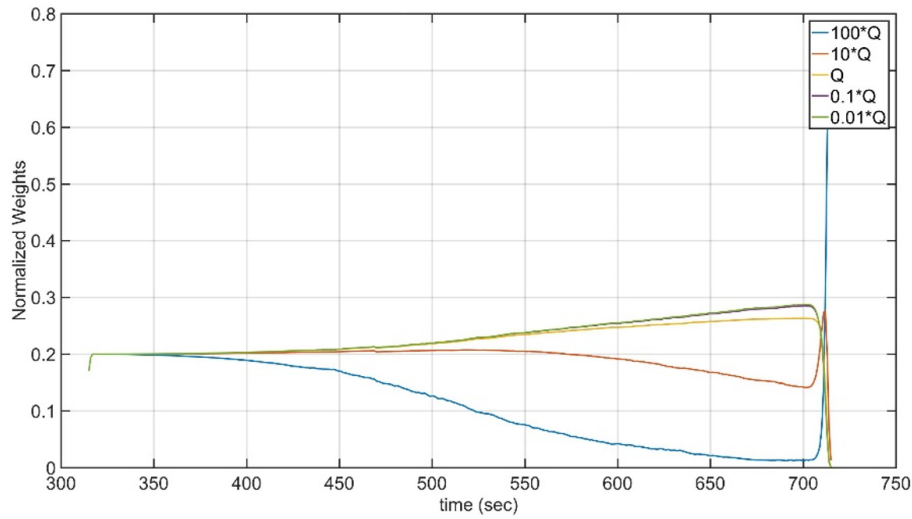
(b)

Figure 13. Model weights for (a) maneuver detection scenario 3 and (b) maneuver detection scenario 4

4.7 Summary

The current study investigates two different adaptive estimation frameworks and their applications to space-based maneuver detection and characterization. The performance of the different adaptive estimation techniques is analyzed through an

extensive parameter study focused on the efficacy of maneuver characterization and state error comparison to non-maneuvering scenarios. The research analysis concludes that a 2G IMM algorithm with VSD filters is reliant on more stringent parameter requirements for convergence, while a 1G IMM algorithm experiences a higher adaptability to changing parameters at the cost of inherently higher state errors. Further research and analysis is required to make conclusions on the dynamical aspects of the IMM algorithms, and entirely new algorithms may be required for optimal performance regarding adaptive estimation.

V. Conclusions and Recommendations

The goals of this study were to investigate adaptive estimation techniques and their applications to space-based maneuver detection and characterization for RPO missions. Overall, the research showed that adaptive estimation algorithms outperform single KF algorithms at detecting and characterizing non-cooperative maneuvers while maintaining similar state errors compared to tracking non-maneuvering targets. The following chapter reviews the research questions answered in this study, the motivation and scope of this study, and concludes with recommendations for future work on this topic.

5.1 Research Questions Answered

The current study was divided into three relevant research questions designed to explore current adaptive estimation techniques and their applications to RPO through an in-depth parameter study and convergence analysis. The following research questions were answered in this study:

- Can adaptive estimation techniques be applied to detect and characterize non-cooperative spacecraft maneuvers in satellite close proximity operations?

  - Section 4.1 shows that a 2G IMM algorithm coupled with VSD filters can detect non-cooperative maneuvers using relative spacecraft dynamics and measurements. Every successful scenario is able to accurately characterize the target maneuver within 1 mm/s^2 of error, all while maintaining state errors comparable to a non-maneuvering scenario. However, varying scenario parameters reveal the sensitivity of the algorithm.

- How do sensor source and type, data rate, maneuver magnitudes, and relative trajectory affect the performance of an adaptive estimation algorithm?

  - Section 4.5 outlines how different scenario parameters appear to be correlated to the performance of both the 1G and 2G IMM algorithms. Overall, the 1G IMM algorithm is able to handle more parameter changes than the 2G IMM algorithm due to the sensitivity of the VSD filters with the PDF, but the 2G IMM algorithm has lower state errors when working properly.

- For what types of scenarios does an adaptive estimation algorithm fail to detect a maneuver or fail to characterize an accurate maneuver magnitude?

  - In relation to the current study, the adaptive estimation algorithm fails to converge in instances of large measurement gaps, large target maneuver magnitudes, and limited types of measurements. The 2G IMM algorithm is especially sensitive to covariance inflation and initial conditions for the VSD filters. Further analysis in Section 4.2 of this research shows that small maneuvers unable to be detected by a 2G IMM algorithm can still be characterized by a 1G IMM algorithm at the cost of higher state errors.

5.2 Research Implications

The motivation behind this research is to aid in the assessment of orbital estimation algorithms with the potential for future use by the USAF to protect space assets through improved SSA. The algorithms demonstrated in this research contributed to the state-of-the-art in orbital estimation by applying maneuver detection and characterization to space-based scenarios. In combination with its

dedicated set of ground-based sensors, the JSpOC can utilize space-based SSA to enhance its space object tracking and lower the chances of creating a UCT due to non-cooperative maneuvers and sensor limitations. Correlating the assessment of adaptive estimation techniques with space-based sensors also aids the USAF space acquisition community in designing better space assets focused on the SSA mission.

The scope of this research focused on space-based applications of adaptive estimation to detect and characterize non-cooperative maneuvers of a target spacecraft in RPO. The current study assumed that the target spacecraft is conducting a continuous, low-thrust maneuver designed to maintain its RPO mission; that initial orbit determination (IOD) of the target has been acquired, which gives the observer adequate information regarding the initial states of the target; and that the target is exhibiting in-plane motion around the observer, further simplifying the problem in order to focus on analyzing the estimation techniques themselves.

This research makes no conclusions on the reason behind any dynamic interaction between the models in each maneuvering scenario, and no optimization scheme was attempted to further improve the adaptive estimation algorithms. The conclusion can simply be made that dynamic, real-time maneuver detection and characterization is further improved in both responsiveness and accuracy by using adaptive estimation. Within the scope of this topic and the assumptions made for this study, the research shows that adaptive estimation techniques can be a viable option for future non-cooperative scenarios where full dynamical knowledge of the target spacecraft is not available.

5.3 Potential Future Research

There are multiple topics and concepts covered in this study that could benefit from further application. A more general RPO scenario requires a full application of three-dimensional nonlinear motion of the target spacecraft relative to the observer. The nonlinear relative satellite motion dynamics are able to more accurately model scenarios without proximity requirements as well as an observer in an elliptical orbit. A full operational application of this research also requires IOD of the target spacecraft and combining space-based with supplemental ground based sensor data, further improving SSA on the target.

Although the current study made viable conclusions on the performance of adaptive estimation techniques for maneuver detection and characterization, the scope of this research barely skimmed the surface on adaptive estimation theory. How and why each model interacts with other models before, during, and after a maneuver requires further investigation which could lead to a better range of dynamic hypotheses for each model. Each IMM algorithm applied in this study also had a fixed number of models with preallocated hypotheses on the dynamics of the system. Further analysis is required to assess how changing the number of models and the range of hypotheses affects performance and responsiveness. Lastly, the IMM algorithms in this study made hypotheses solely on the process noise covariance applied to the system dynamics, but the IMM framework can be designed to make any number of hypotheses based on the uncertainty of the maneuvering target. Useful future applications of the IMM algorithm may involve assessing different ranges of sensor noise or even making guesses at the thrust vector of the target.

Another area of potential future work involves applying adaptive estimation to a variety of different target maneuvers that represent more realistic RPO missions.

Section 4.4 assesses the performance of the 1G IMM algorithm with a dynamic thrust vector, but the estimator still assumes that the maneuver states remain constant throughout the scenario. Although most space-based thrusters exhibit a constant force, the perceived acceleration of the target relative to the observer changes with respect to the propellant burned by the target. The dynamic thrust scenarios showed that adaptive estimation techniques may not be sufficient if the thrust vector is assumed to be constant, so information must be fed into the filter that allows the estimation technique to predict the maneuver magnitude with respect to the assumed mass of the target spacecraft.

Along with the assumptions regarding the maneuver magnitude, the adaptive estimation techniques demonstrated in this research requires further study into other realistic RPO missions. This study simply applied a constant maneuver for a predetermined period of time to the target without any mission goals in mind. A more realistic maneuver detection scenario takes into account a certain mission objective for both the target and the observer as well as gaps in measurement data where sensors are blocked by the Sun vector or in eclipse.

5.4   Conclusion

The research demonstrated herein investigates different adaptive estimation techniques and their applications in non-cooperative maneuver detection and characterization of target spacecraft operating in close proximity to an observer spacecraft. Adaptive estimation utilizes a bank of filters with different hypotheses on a system's dynamics to account for unexpected changes in the dynamical model. Combined with a series of VSD filters, the adaptive estimation algorithm is able to detect and track target maneuvers of reasonable magnitude given a high rate of measurement data. A more classical adaptive estimation approach is able to

79

characterize maneuvers with a wider variety of changing scenario parameters at the cost of a small increase in estimated state errors. Overall, adaptive estimation is a vast area of research with a variety of useful applications to the space-based SSA mission of the USAF.

Appendix A. Estimation Algorithms

Algorithm 1: Extended Kalman Filter

---

1 Initialize or define previous state and covariance: $\hat{\mathbf{x}}_0$, $\hat{\mathbf{P}}_0$ or $\hat{\mathbf{x}}_{i-1}$, $\hat{\mathbf{P}}_{i-1}$

2 Propagate state from t_{i-1} to t_i to determine $\overline{\mathbf{x}}_i$ and $\boldsymbol{\Phi}(t_i, t_{i-1})$

      Initial condition: $\hat{\mathbf{x}}_{i-1}$ Differential eq: $\dot{\mathbf{x}} = f(\mathbf{x}, t)$

      Initial condition: $\boldsymbol{\Phi}(t_{i-1}, t_{i-1}) = \mathbf{I}$ Differential eq: $\dot{\boldsymbol{\Phi}} = \frac{\partial f(\mathbf{x}, t)}{\partial \mathbf{x}} \boldsymbol{\Phi}(t_i, t_{i-1})$

3 Update covariance:

$$\overline{\mathbf{P}}_i = \boldsymbol{\Phi}(t_i, t_{i-1}) \hat{\mathbf{P}}_{i-1} \boldsymbol{\Phi}(t_i, t_{i-1})^T + \mathbf{Q}_i$$

4 Read in observation and sensor noise at t_i: $\mathbf{y}_i$, $\mathbf{R}_i$

5 Calculate the measurement basis function and residuals:

$$\mathbf{H}_i = \frac{\partial G(\overline{\mathbf{x}}_i, t)}{\partial \mathbf{x}} \qquad \nu_i = \mathbf{y}_i - G(\overline{\mathbf{x}}_i, t_i)$$

6 Calculate the observation covariance and mahalanobis distance:

$$\mathbf{S}_i = \mathbf{H}_i \overline{\mathbf{P}}_i \mathbf{H}_i^T + \mathbf{R}_i \qquad \Psi_i = \nu_i^T \mathbf{S}_i^{-1} \nu_i$$

7 Use the Kalman gain to correct the updated state and covariance:

$$\mathbf{K}_i = \overline{\mathbf{P}}_i \mathbf{H}_i^T \mathbf{S}_i^{-1} \qquad \hat{\mathbf{x}}_i = \overline{\mathbf{x}}_i + \mathbf{K}_i \nu_i \qquad \hat{\mathbf{P}}_i = (\mathbf{I} - \mathbf{K}_i \mathbf{H}_i) \overline{\mathbf{P}}_i$$

8 Return to step 1, process observation at t_{i+1}

Algorithm 2: Unscented Kalman Filter

Given: pre-defined weights κ, w_m^j, and w_c^j for $j = 1,...,2n$

1 Initialize or define previous state and covariance: $\hat{\mathbf{x}}_0$, $\hat{\mathbf{P}}_0$ or $\hat{\mathbf{x}}_{i-1}$, $\hat{\mathbf{P}}_{i-1}$

2 Perform decomposition $\hat{\mathbf{P}}_{i-1} = \mathbf{A}^T\mathbf{A}$; denote $\mathbf{a}^j$ as column $j = 1,...,n$ of $\mathbf{A}$

3 Calculate sigma points:

$$\tilde{\mathbf{x}}_{i-1}^j = \mathbf{x}_{i-1} + \breve{\mathbf{x}}^j \quad \text{for } j = 0,...,2n \qquad \breve{\mathbf{x}}^0 = 0$$

$$\breve{\mathbf{x}}^j = \mathbf{a}^j\sqrt{n+\kappa} \quad \text{for } j = 1,...,n \qquad \breve{\mathbf{x}}^{n+j} = -\mathbf{a}^j\sqrt{n+\kappa} \quad \text{for } j = 1,...,n$$

4 Propagate all sigma points from t_{i-1} to t_i:

Initial condition: $\tilde{\mathbf{x}}_{i-1}^j$ 　　　Differential eq: $\dot{\mathbf{x}} = f(\mathbf{x}, t)$

Propagated results: $\tilde{\mathbf{x}}_i^j$

5 Calculate propagated state and covariance:

$$\overline{\mathbf{x}}_i = \sum_{j=0}^{2n} w_m^j\tilde{\mathbf{x}}_i^j \qquad \overline{\mathbf{P}}_i = \sum_{j=0}^{2n} w_c^j\left(\tilde{\mathbf{x}}_i^j - \overline{\mathbf{x}}_i\right)\left(\tilde{\mathbf{x}}_i^j - \overline{\mathbf{x}}_i\right)^T + \mathbf{Q}_i$$

6 Transform sigma points and calculate predicted observation:

$$\tilde{\mathbf{y}}_i^j = G\left(\tilde{\mathbf{x}}_i^j, t_i\right) \qquad \hat{\mathbf{y}}_i = \sum_{j=0}^{2n} w_m^j\tilde{\mathbf{y}}_i^j$$

7 Read in measurement and sensor noise at t_i: $\mathbf{y}_i$, $\mathbf{R}_i$

8 Calculate the observation covariance, residuals, and mahalanobis distance:

$$\mathbf{S}_i = \sum_{j=0}^{2n} w_c^j\left(\tilde{\mathbf{y}}_i^j - \hat{\mathbf{y}}_i\right)\left(\tilde{\mathbf{y}}_i^j - \hat{\mathbf{y}}_i\right)^T + \mathbf{R}_i$$

$$\nu_i = \mathbf{y}_i - \hat{\mathbf{y}}_i \qquad \mathbf{\Psi} = \nu_i^T\mathbf{S}_i^{-1}\nu_i$$

9 Use the Kalman gain to correct the updated state and covariance:

$$\mathbf{V}_i = \sum_{j=0}^{2n} w_c^j\left(\tilde{\mathbf{x}}_i^j - \hat{\mathbf{x}}_i\right)\left(\tilde{\mathbf{y}}_i^j - \hat{\mathbf{y}}_i\right)^T \qquad \mathbf{K}_i = \mathbf{V}_i\mathbf{S}_i^{-1}$$

$$\hat{\mathbf{x}}_i = \overline{\mathbf{x}}_i + \mathbf{K}_i\nu_i \qquad\qquad \hat{\mathbf{P}}_i = \overline{\mathbf{P}}_i - \mathbf{K}_i\mathbf{S}_i\mathbf{K}_i^T$$

10 Return to step 1, process observation at t_{i+1}

Algorithm 3: Interacting Multiple Model

1 Determine mixing probabilities at time of next observation, t_i:

$$\bar{\mathbf{c}}_k = \sum_{j=1}^{N} \mathbf{Pr}_{j|k} \mathbf{w}_{i-1}^{j} \text{ for each model k up to } N \text{ models}$$

$$\mathbf{w}_{i-1}^{j|k} = \frac{1}{\bar{\mathbf{c}}_k} \mathbf{Pr}_{j|k} \mathbf{w}_{i-1}^{j} \text{ for all } N^2 \text{ model combinations}$$

2 Determine the individual state and covariance for each model k:

$$\tilde{\mathbf{x}}_{i-1}^{k} = \sum_{j=1}^{N} \hat{\mathbf{x}}_{i-1}^{j} \mathbf{w}_{i-1}^{j|k}$$

$$\tilde{\mathbf{P}}_{i-1}^{k} = \sum_{j=1}^{N} \mathbf{w}_{i-1}^{j|k} \left[\hat{\mathbf{P}}_{i-1}^{j} + \left(\hat{\mathbf{x}}_{i-1}^{j} - \tilde{\mathbf{x}}_{i-1}^{k} \right) \left(\hat{\mathbf{x}}_{i-1}^{j} - \tilde{\mathbf{x}}_{i-1}^{k} \right)^{T} \right]$$

3 Input $\tilde{\mathbf{x}}_{i-1}^{k}$ and $\tilde{\mathbf{P}}_{i-1}^{k}$ into each filter k, propagate and update the estimated state, covariance, residual, and observation covariance through each individual model: $\hat{\mathbf{x}}_{i}^{k}$, $\hat{\mathbf{P}}_{i}^{k}$, ν_{i}^{k}, and $\mathbf{S}_{i}^{k}$.

4 Update the likelihood change and updated weight for each model using the probability density function:

$$\Lambda_{i}^{k} = \mathcal{N}\left(\nu_{i}^{k}; 0, \mathbf{S}_{i}^{k} \right) = \frac{1}{\sqrt{|2\pi\mathbf{S}_{i}^{k}|}} e^{\frac{-1}{2} \left(\nu_{i}^{k} \right)^{T} \left(\mathbf{S}_{i}^{k} \right)^{-1} \nu_{i}^{k}} \qquad \mathbf{w}_{i}^{k} = \frac{\Lambda_{i}^{k} \bar{\mathbf{c}}_k}{\sum_{j=1}^{N} \Lambda_{i}^{j} \bar{\mathbf{c}}_j}$$

5 Calculate weighted estimates:

$$\underline{\mathbf{x}}_{i} = \sum_{k=1}^{N} \hat{\mathbf{x}}_{i}^{k} \mathbf{w}_{i}^{k} \qquad \underline{\mathbf{\Psi}}_{i} = \sum_{k=1}^{N} \mathbf{w}_{i}^{k} \mathbf{\Psi}_{i}^{k}$$

$$\underline{\mathbf{P}}_{i} = \sum_{k=1}^{N} \mathbf{w}_{i}^{k} \left[\hat{\mathbf{P}}_{i}^{k} + \left(\hat{\mathbf{x}}_{i}^{k} - \underline{\mathbf{x}}_{i} \right) \left(\hat{\mathbf{x}}_{i}^{k} - \underline{\mathbf{x}}_{i} \right)^{T} \right]$$

6 Return to step 1, process observation at t_{i+1}

Appendix B. Additional Scenarios and Results

In stochastic estimation, there is a trade off between not having enough data for statistical relevance and having too much data that distracts from the claims made by the research. The following results are additional scenarios that emphasize the claims made in Chapter 4 without inflating the main body of the work.

Maneuver detection scenarios 3 and 4 show successful detections of average target maneuver magnitudes. Maneuver detection scenario 4 shows that the 2G IMM algorithm still works given poor sensor measurements with an inflated initial process noise covariance.

Table 20. Initial parameters for maneuver detection scenario 3

Parameter	Value
Thrust acceleration (mm/s^2)	10
Thrust duration (s)	100
Scenario length (s)	1500
Initial relative trajectory (m)	1000
Data rate (sec^{-1})	1
Data type	$[\rho\ \alpha]$
Sensor Quality	good
Q_0	1×10^{-10}

Table 21. Simulation results for maneuver detection scenario 3

RMSE	IMM UKF
δx (m)	0.035
δy (m)	0.16
$\delta\dot{x}$ (m/s)	2.0×10^{-3}
$\delta\dot{y}$ (m/s)	0.048
δT (m/s^2)	2.99×10^{-3}
Man start (s)	2.86
Man duration (s)	0.87

Table 22. Initial parameters for maneuver detection scenario 4

Parameter	Value
Thrust acceleration (mm/s^2)	50
Thrust duration (s)	400
Scenario length (s)	1500
Initial relative trajectory (m)	1000
Data rate (sec^{-1})	1
Data type	$[\rho \; \alpha]$
Sensor Quality	poor
Q$_0$	1×10^{-5}

Table 23. Simulation results for maneuver detection scenario 4

RMSE	IMM UKF
δx (m)	1.09
δy (m)	0.44
$\delta\dot{\text{x}}$ (m/s)	0.070
$\delta\dot{\text{y}}$ (m/s)	0.10
δT (m/s^2)	8.62×10^{-4}
Man start (s)	13.83
Man duration (s)	3.45

Small maneuver scenario 1 has no significant difference in error between the single filter and IMM filters.

Table 24. Simulation results for small maneuver scenario 1

RMSE	Single UKF	Single EKF	IMM UKF	IMM EKF
δx (m)	0.56	0.36	0.098	0.64
δy (m)	3.45	0.75	0.76	1.42
$\delta\dot{\text{x}}$ (m/s)	8.6×10^{-3}	0.061	2.9×10^{-3}	0.064
$\delta\dot{\text{y}}$ (m/s)	0.056	0.27	0.026	0.28

Maneuver characterization scenario 4 has a harder time characterizing a large maneuver with poor sensors, but RMSE values are along the same lines as other scenarios with poor sensors.

Table 25. Initial parameters for maneuver characterization scenario 4

Parameter	Value
Thrust acceleration $(\mathrm{mm/s^2})$	100
Thrust duration (s)	100
Scenario length (s)	1500
Initial relative trajectory (m)	1000
Data rate $(\sec^{-1})$	10
Data type	$[\rho\ \alpha]$
Sensor Quality	poor
Q_0	1×10^{-7}

Table 26. Simulation results for maneuver characterization scenario 4

RMSE	Single UKF	Single EKF	IMM UKF	IMM EKF
δx (m)	11.70	25.56	4.03	9.60
δy (m)	21.74	3.47	2.17	6.27
$\delta\dot{\mathrm{x}}$ (m/s)	0.20	0.14	0.087	2.37
$\delta\dot{\mathrm{y}}$ (m/s)	1.08	3.52	0.34	1.68
$\mathrm{T_x}$ $(\mathrm{m/s^2})$	2.0×10^{-3}	3.6×10^{-4}	1.6×10^{-3}	6.0×10^{-3}
$\mathrm{T_y}$ $(\mathrm{m/s^2})$	0.30	0.028	0.022	0.027

Two more dynamic thrust scenarios show similar RMSE values and maneuver characterization success.

Table 27. Simulation results for dynamic thrust scenario 2

RMSE	IMM UKF
δx (m)	46.70
δy (m)	45.58
$\delta\dot{x}$ (m/s)	0.31
$\delta\dot{y}$ (m/s)	0.32
T_x (m/s^2)	0.0016
T_y (m/s^2)	0.0024

Table 28. Simulation results for dynamic thrust scenario 3

RMSE	IMM UKF
δx (m)	39.14
δy (m)	41.78
$\delta\dot{x}$ (m/s)	0.25
$\delta\dot{y}$ (m/s)	0.27
T_x (m/s^2)	0.0012
T_y (m/s^2)	0.0011

Appendix C. Nonlinear Dynamical Analysis

Based on preliminary analysis, Section 4.5 claims that the relative trajectory assumption for the HCW equations of motion becomes invalid before the adaptive estimation algorithm diverges. The relative trajectory parameter is not a primary focus in this study because a large distance between the observer and the target degrades the analysis for this study with respect to RPO scenarios.

The following scenario has the same initial conditions and uses a 2G IMM algorithm for maneuver detection, but one IMM algorithm propagates the state vector using the linearized HCW equations of motion (Equation (2.15)), while the other IMM algorithm propagates the state vector using the nonlinear HCW equations of motion without the relative trajectory assumption (Equation (2.17)). Table 29 shows the initial conditions for the scenario, while Table 30 shows the results for the scenario.

Table 29. Initial parameters for the relative trajectory scenario

Parameter	Value
Thrust acceleration (mm/s^2)	30
Thrust duration (s)	100
Scenario length (s)	1500
Initial relative trajectory (m)	1.0×10^5
Data rate (sec^{-1})	1
Data type	$[\rho \; \alpha]$
Sensor Quality	good
Q_0	1×10^{-12}

Based on results in Table 30, the dynamics appear to worsen the estimated state vector, but the 2G IMM algorithm still detects a maneuver with seconds of

error. The higher RMSE values could be attributed to the large relative trajectory, which adds noise to the range measurements themselves, or the degraded dynamics at large relative trajectories, which seems counter intuitive for this scenario because the nonlinear dynamics produce higher RMSE values than the linear dynamics.

Table 30. Simulation results for the relative trajectory scenario

RMSE	Linear IMM UKF	Nonlinear IMM UKF
δx (m)	7.08	44.24
δy (m)	43.89	326.22
$\delta \dot{x}$ (m/s)	0.039	0.12
$\delta \dot{y}$ (m/s)	0.57	1.16
Man start (s)	0.99	0.99
Man duration (s)	1.33	4.71

Bibliography

[1] B. J. Weichert, "The High Ground: The Case for U.S. Space Dominance," *Orbis*, vol. 61, no. 2, pp. 227–237, 2017.

[2] National Research Council, *Continuing Kepler's Quest Assessing Air Force Space Command's Astrodynamics Standards*. The National Academies Press, 2012.

[3] Department of Defense & Office of the Director of National Intelligence, *National Security Space Strategy Unclassified Summary*. 2011.

[4] United Nations General Assembly, "Report of the Committe on the Peaceful Uses of Outer Space," 1975.

[5] M. Wasson, "Space Situational Awareness in the Joint Space Operations Center," *Advanced Maui Optical and Space Surveillance Conference*, vol. 298, no. 0704, pp. 8–10, 2011.

[6] M. A. Baird, "Maintaining Space Situational Awareness and Taking it to the Next Level," *Air and Space Power Journal*, vol. 27, no. 5, pp. 50–72, 2013.

[7] G. M. Goff, *Orbit Estimation of Non-Cooperative Maneuvering Spacecraft*. PhD thesis, Air Force Institute of Technology, 2015.

[8] G. M. Goff, J. T. Black, and J. A. Beck, "Orbit Estimation of a Continuously Thrusting Spacecraft Using Variable Dimension Filters," *Journal of Guidance, Control, and Dynamics*, vol. 38, no. 12, pp. 2407–2420, 2015.

[9] W. E. Wiesel, *Modern Orbit Determination*. Beavercreek, Ohio: Aphelion Press, 2nd ed., 2010.

[10] C. F. Gauss, *Theory of the Motion of the Heavenly Bodies Moving about the Sun in Conic Sections*. Mieola, NY: Dover Publications, 1857.

[11] B. D. Tapley, B. E. Schutz, and G. H. G. H. Born, *Statistical Orbit Determination*. Burlington, MA: Elsevier Academic Press, 1st ed., 2004.

[12] R. F. Stengel, *Optimal Control and Estimation*. New York, NY: Dover Publications, 1994.

[13] U. P. Desai, *A Comparative Study of Estimation Models for Satellite Relative Motion*. PhD thesis, Texas A&M University, 2013.

[14] H. W. Sorenson, "Least-squares estimation: from Gauss to Kalman," *IEEE Spectrum*, vol. 7, no. 7, pp. 63–68, 1970.

[15] David A. Vallado, *Fundamentals of Astrodynamics and Applications.* Hawthorne, CA: Microcosm Press, 4th ed., 2013.

[16] D. Vallado and P. Crawford, "SGP4 Orbit Determination," *AIAA/AAS Astrodynamics Specialist Conference and Exhibit*, no. August, pp. 18–21, 2008.

[17] R. E. Kalman, "A New Approach to Linear Filtering and Prediction Problems," *Journal of Basic Engineering*, vol. 82, no. 1, 1960.

[18] J. R. Wright, "Optimal orbit determination," in *Advances in the Astronautical Sciences*, vol. 112 II, pp. 1123–1134, 2002.

[19] G. Welch and G. Bishop, "An Introduction to the Kalman Filter," *University of North Carolina*, vol. 7, no. 1, pp. 1–16, 2006.

[20] S. J. Julier and J. K. Uhlmann, "A New Extension of the Kalman Filter to Nonlinear Systems," *11th Symposium on Aerospace/Defense Sensing (AeroSense), Simulations and Controls*, 1997.

[21] S. J. Julier and J. K. Uhlmann, "Unscented filtering and Nonlinear Estimation," in *Proceedings of the IEEE*, vol. 92, pp. 401–422, 2004.

[22] B. O. Teixeira, M. A. Santillo, R. S. T. Erwin, and D. S. Bernstein, "Spacecraft Tracking Using Sampled-Data kalman filters," *IEEE Control Systems*, vol. 28, no. 4, pp. 78–94, 2008.

[23] P. C. P. M. Pardal, H. K. Kuga, and R. V. de Moraes, "Robustness assessment between sigma point and extended Kalman filter for orbit determination," *Journal of Aerospace Engineering, Sciences and Applications*, vol. 3, no. 3, pp. 35–44, 2011.

[24] J. R. Wright and J. Woodburn, "Nonlinear Variable Lag Smoother," *Advances in the Astronautical Sciences*, vol. 132, pp. 745–764, 2008.

[25] R. E. Helmick, W. D. Blair, and S. A. Hoffman, "Fixed-Interval Smoothing for Markovian Switching Systems," *IEEE Transactions on Information Theory*, vol. 41, no. 6, pp. 1845–1855, 1995.

[26] S. Sarkka, "Unscented Rauch Tung Striebel Smoother," *IEEE Transactions on Automatic Control*, vol. 53, no. 3, pp. 845–849, 2008.

[27] D. Magill, "Optimal adaptive estimation of sampled stochastic processes," *IEEE Transactions on Automatic Control*, vol. 10, no. 4, pp. 434–439, 1965.

[28] W. C. Li, P. Wei, and X. C. Xiao, "An adaptive nonlinear filter of discrete-time system with uncertain covariance using unscented kalman filter," *ISCIT 2005 - International Symposium on Communications and Information Technologies 2005, Proceedings*, vol. I, pp. 1389–1392, 2005.

[29] R. L. Moose, "An Adaptive State Estimation Solution to the Maneuvering Target Problem," *IEEE Transactions on Automatic Control*, vol. 20, no. 3, pp. 359–362, 1975.

[30] X. R. Li and V. P. Jilkov, "Survey of Maneuvering Target Tracking. Part V: Multiple-Model Methods," *IEEE Transactions on Aerospace and Electronic Systems*, vol. 41, no. 4, pp. 1255–1321, 2005.

[31] D. A. Vallado and J. H. Seago, "Covariance Realism," in *AAS/AIAA Astrodynamics Specialist Conference*, (Pittsburgh, PA), pp. 1–19, 2009.

[32] H. A. P. Blom and Y. Bar-Shalom, "The Interacting Multiple Model Algorithm for Systems with Markovian Switching Coefficients," *IEEE Transactions on Automatic Control*, vol. 33, no. 8, pp. 780–783, 1988.

[33] Y. Bar-Shalom and K. Birmiwal, "Variable Dimension Filter for Maneuvering Target Tracking," *IEEE Transactions on Aerospace and Electronic Systems*, vol. AES-18, no. 5, pp. 621–629, 1982.

[34] T. K. Yaakov Bar-Shalom, X. Rong LI, *Estimation with Applications to Tracking and Navigation*. New York, NY: John Wiley & Sons, Inc., 2001.

[35] R. De Maesschalck, D. Jouan-Rimbaud, and D. L. Massart, "The Mahalanobis distance," *Chemometrics and Intelligent Laboratory Systems*, vol. 50, no. 1, pp. 1–18, 2000.

[36] G. W. Hill, "Researches in the Lunar Theory," *American Journal of Mathematics*, vol. 1, no. 1, 1878.

[37] W. H. Clohessy and R. S. Wiltshire, "Terminal Guidance System for Satellite Rendezvous," *Journal of the Aerospace Sciences*, vol. 27, no. 9, pp. 653–658, 1960.

[38] W. E. Wiesel, *Spaceflight Dynamics*. Beavercreek, Ohio: Aphelion Press, 3rd ed., 2010.

[39] R. Bate, D. Mueller, and J. White, *Fundamentals of Astrodynamics*. 1971.

[40] T. A. Lovell and S. Tragesser, "Guidance for Relative Motion of Low Earth Orbit Spacecraft Based on Relative Orbit Elements," *AIAA/AAS Astrodynamics Specialist Conference and Exhibit*, no. August, pp. 1–16, 2004.

[41] C. Doolittle, F. Chavez, and T. A. Lovell, "Relative Orbit Element Estimation for Satellite Navigation," *AIAA Guidance, Navigation, and Control Conference and Exhibition*, no. August, pp. 1–11, 2005.

[42] P. R. Escobal, *Methods of Orbit Determination*. New York, NY: J. Wiley, 1965.

[43] G. Gaias, S. D'Amico, and J.-S. Ardaens, "Angles-Only Navigation to a Noncooperative Satellite Using Relative Orbital Elements," *Journal of Guidance, Control, and Dynamics*, vol. 37, no. 2, pp. 439–451, 2014.

[44] J. L. Junkins, D. C. Hughes, K. P. Wazni, and V. Pariyapong, "Vision-Based Navigation for Rendezvous , Docking and Proximity Operation," no. February, pp. 24–28, 1999.

[45] M. P. Whittaker, R. Linares, and J. L. Crassidis, "Photometry and Angles Data for Spacecraft Relative Navigation," *AIAA Guidance, Navigation, and Control (GNC) Conference*, pp. 1–17, 2013.

[46] U. Krutz, H. Jahn, E. K??hrt, S. Mottola, and P. Spietz, "Radiometric considerations for the detection of space debris with an optical sensor in LEO as a secondary goal of the AsteroidFinder mission," *Acta Astronautica*, vol. 69, no. 5-6, pp. 297–306, 2011.

[47] H. B. Hablani, "Laser Range Finder Closed-Loop Pointing Technology of Relative Navigation, Attitude Determination, Pointing and Tracking for Spacecraft Rendezvous.pdf," 2004.

[48] H. Evans, J. Lange, and J. Schmitz, *The Phenomenology of Intelligence-focused Remote Sensing*. New York, NY: Riverside Research, 2014.

[49] C. Weitkamp, *Lidar: Range-Resolved Optical Remote Sensing of the Atmosphere*. New York, NY: Springer Science and Business Media, Inc., 2005.

[50] J. R. Wertz, D. F. Everett, and J. J. Puchell, *Space Mission Engineering: The New SMAD*. Hawthorne, CA: Microcosm Press, 2011.

[51] D. Simon, *Optimal State Estimation*. Hoboken, NJ: John Wiley & Sons, Inc., 2006.